

1 **Title: Plant mixed lineage kinase domain-like proteins limit biotrophic**  
2 **pathogen growth**

3

4 **One Sentence Summary: Plants have a protein family that is**  
5 **structurally homologous to vertebrate mixed lineage kinase domain-**  
6 **like protein, which induces necroptotic cell death, but these plant**  
7 **proteins can confer immunity without host cell death.**

8

9 **Short title: Plant MLKLs confer disease resistance**

10 **Authors:** Lisa Mahdi<sup>\*1,2</sup>, Menghang Huang<sup>\*3</sup>, Xiaoxiao Zhang<sup>\*3</sup>, Ryohei  
11 Thomas Nakano<sup>1,4</sup>, Leïla Brulé Kopp<sup>1,5</sup>, Isabel M.L. Saur<sup>1</sup>, Florence Jacob<sup>1,6,7</sup>,  
12 Viera Kovacova<sup>8,9</sup>, Dmitry Lapin<sup>1</sup>, Jane E. Parker<sup>1,4</sup>, James M. Murphy<sup>10,11</sup>,  
13 Kay Hofmann<sup>12</sup>, Paul Schulze-Lefert<sup>1,4</sup>, Jijie Chai<sup>1,3,4</sup> and Takaki Maekawa<sup>1, †</sup>

14 \*These authors contributed equally

15 <sup>1</sup>Max Planck Institute for Plant Breeding Research, 50829 Cologne, Germany

16 <sup>2</sup>Current address, Botanical Institute, Cologne Biocenter, University of Cologne, Cologne, 50674,  
17 Germany.

18 <sup>3</sup>Beijing Advanced Innovation Center for Structural Biology, Tsinghua-Peking Joint Center for Life  
19 Sciences, Center for Plant Biology, School of Life Sciences, Tsinghua University, 100084 Beijing, China.

20 <sup>4</sup>Cluster of Excellence on Plant Sciences (CEPLAS), Max Planck Institute for Plant Breeding Research,  
21 50829 Cologne, Germany

22 <sup>5</sup>Ecole normale supérieure Paris, F-75230 Paris cedex 05

23 <sup>6</sup>Institute of Plant Sciences Paris-Saclay, Centre National de la Recherche Scientifique, Institut National  
24 de la Recherche Agronomique, Université Paris-Sud, Université d'Evry, Université Paris-Diderot,  
25 Sorbonne Paris-Cité, Université Paris-Saclay, 91405 Orsay, France

26 <sup>7</sup>Current address, PalmElit SAS, F-34980 Montferrier-sur-Lez, France

27 <sup>8</sup>University of Cologne, Cologne Excellence Cluster on Cellular Stress Responses in Aging-Associated  
28 Diseases (CECAD), University of Cologne, 50931 Cologne, Germany.

29 <sup>9</sup>Current address: Institute for Biological Physics, University of Cologne, Cologne, 50937, Germany.

30 <sup>10</sup>Walter and Eliza Hall Institute of Medical Research, 1G Royal Parade, Parkville, VIC 3052, Australia;

31 <sup>11</sup>Department of Medical Biology, University of Melbourne, Parkville, VIC 3052, Australia.

32 <sup>12</sup>Institute for Genetics, University of Cologne, 50674 Cologne, Germany

33 <sup>†</sup>Corresponding author. Email: [maekawa@mpipz.mpg.de](mailto:maekawa@mpipz.mpg.de) (T.M.)

34

34 **Abstract:**

35 Mixed lineage kinase domain-like (MLKL) protein mediates necroptotic cell  
36 death in vertebrates. We report here the discovery of a conserved protein  
37 family across seed plants that is structurally homologous to vertebrate  
38 MLKL. The *Arabidopsis thaliana* genome encodes three MLKLs with  
39 overlapping functions in limiting growth of obligate biotrophic fungal and  
40 oomycete pathogens. Although displaying a cell death activity mediated by N-  
41 terminal helical bundles, termed HeLo domain, *At*MLKL-dependent immunity  
42 can be separated from host cell death. Cryo-electron microscopy structures of  
43 *At*MLKLs reveal a tetrameric configuration, in which the pseudokinase domain  
44 and brace region bury the HeLo-domains, indicative of an auto-repressed  
45 complex. We also show the association of two *At*MLKLs with microtubules.  
46 These findings, coupled with resistance-enhancing activity and altered  
47 microtubule association of a phosphomimetic mutation in the pseudokinase  
48 domain of *At*MLKL1, point to a cell death-independent immunity mechanism.

49

49 **Main text:**

50 Regulated cell death (RCD) is intimately connected with innate immunity in  
51 plants and animals (1-3). A shared feature of several proteins involved in RCD  
52 in plants, animals and fungi is a four-helical bundle structure called the HeLo-  
53 domain (4). HeLo domain-containing MLKL (mixed lineage kinase domain-like  
54 protein) mediates necroptosis in animals (5, 6), a form of RCD that is  
55 proposed to combat pathogens by releasing pro-inflammatory molecules (7,  
56 8). Necroptosis is initiated by the plasma membrane (PM)-resident death  
57 receptors, with downstream activation of receptor-interacting  
58 serine/threonine-protein kinases (RIPKs) leading to the phosphorylation of the  
59 pseudokinase domain of the terminal pathway effector, MLKL (7, 8). This  
60 process assembles monomeric MLKL into pro-necroptotic oligomers (9) that  
61 translocate to the PM where oligomerized HeLo-domains interfere with  
62 membrane integrity (10-14). The extent to which RCD in plants and animals is  
63 directly responsible for disease resistance is under debate (3, 15-17).

64

65 To identify novel immune regulators in plants, we searched for HeLo domain-  
66 containing proteins in plant genomes by comparing Hidden Markov Models.  
67 This analysis identified a protein family that is highly conserved across plants  
68 (Fig. 1, Table S1, Supplemental file 1), with a modular structure resembling  
69 MLKL (Fig. 1A). The kinase-like domain lacks canonical residues known to  
70 underlie phosphoryl transfer (18) (Fig. 1B), suggestive of a catalytically  
71 inactive pseudokinase (8). Hereafter, we refer to these proteins as plant  
72 MLKLs. Plant MLKLs additionally possess an extended serine-rich region of  
73 varying length after the pseudokinase domain without similarity to any known

74 domain (Fig. 1A, Supplemental file 1). Plant MLKLs separate into two  
75 subgroups based on sequence similarity (Fig. 1D). *Arabidopsis thaliana*  
76 harbours three *MLKL* genes with *AtMLKL1* and *AtMLKL2* in subfamily I and  
77 *AtMLKL3* belonging to subfamily II (Fig. 1D).

78

79 To explore similarities between plant and animal MLKLs, we expressed  
80 *AtMLKL2* and *AtMLKL3* for structural analysis using cryo-electron microscopy  
81 (Fig. 2, Fig. S1 and S2). In gel filtration, both proteins eluted at an estimated  
82 molecular weight corresponding to tetramers (Fig. 2A, Fig. S2A). This  
83 contrasts with the vertebrate MLKL protein, which displayed heterogeneity in  
84 a similar assay (13). Representative 2D projection views indicate that both  
85 *AtMLKL* oligomers form a triangle-like architecture with a 2-fold symmetry (Fig.  
86 S1AB, Fig. S2BC). Further 3D classification and refinement generated density  
87 maps of oligomeric *AtMLKL2* and *AtMLKL3* with a global resolution of 4.1Å  
88 (Fig. S2E) and 3.4Å (Fig. S1D) respectively, based on the gold Fourier Shell  
89 Correlation standard (Fig. S1C, Fig. S2D). The 3D reconstructions show that  
90 both *AtMLKL2* and *AtMLKL3* oligomers are composed of four MLKL  
91 molecules (Fig. 2C, Fig. S3A), confirming that these form tetramers.  
92 Tetramerization of *AtMLKL2* or *AtMLKL3* results in formation of a pyramid-like  
93 structure. Structure alignment of the two final models indicates that tetramers  
94 of two subfamily members are nearly identical (Fig. S3AB). As the quality of  
95 the density of *AtMLKL3* is superior for model building, we limited our structural  
96 analysis to *AtMLKL3*.



97 The N-terminal HeLo domain of *At*MLKL3 forms a four-helix bundle (Fig. S3C)  
98 which superimposed well with the HeLo domains of mouse and human MLKL  
99 (mMLKL and hMLKL, respectively; Fig. 2D). This observation supports the  
100 idea that *At*MLKL3 is a bona fide homolog of vertebrate MLKLs. Nevertheless,  
101 compared to mMLKL, the HeLo domain of *At*MLKL3 packs tightly against its  
102 pseudokinase domain (Fig. S3D). The packing is further strengthened by the  
103 brace region of *At*MLKL3, which contains a string of five helices that  
104 simultaneously interact with the HeLo and pseudokinase domains (Fig. S3C).  
105 The HeLo domains and the brace regions form the core of the *At*MLKL3  
106 tetramer, whereas the pseudokinase domains are presented at the apices of  
107 the pyramid-like structure (Fig. 2C). Hydrophobic packing of  $\alpha$ 1 helices (Fig.  
108 S3E) from two *At*MLKL3 molecules contributes to formation of a homodimeric  
109 *At*MLKL3. In the tetrameric *At*MLKL3, the two  $\alpha$ 1-mediated homodimers pack  
110 perpendicularly to each other (Fig. 2G). Four brace regions, which are  
111 positioned nearly in the same plane, are sandwiched between the two  
112 homodimers and exclusively mediate homodimer-homodimer interaction (Fig.  
113 2F). The N-terminal halves of the four brace regions form two homodimer  
114 pairs, and the C-terminal halves another two pairs (Fig. S3E). The  
115 intermolecular interactions lead to further sequestering of the *At*MLKL3 N-  
116 terminal HeLo domain. Taken together, our observations indicate that  
117 *At*MLKL3 is a structural homolog of vertebrate MLKLs and its N-terminal HeLo  
118 domain is sequestered through both intra- and intermolecular interactions.

119

120 To determine the role of plant MLKLs in immunity, we challenged  
121 combinatorial loss-of-function mutants of *At*MLKLs (Fig. S4) with different

122 microbial pathogens. *Atmlkl* single mutants exhibited increased susceptibility  
123 to the obligate biotrophic fungus *Golovinomyces orontii* compared to wild-type  
124 plants and, strikingly, the triple mutant was as susceptible as an *eds1* mutant  
125 (Fig. 3A), which is hyper-susceptible to a number of pathogens including the  
126 obligate biotrophic oomycete *Hyaloperonospora arabidopsidis* (*Hpa*). The  
127 immune response restricting *Golovinomyces* growth in Col-0 wild-type plants  
128 is not associated with host cell death (19). In *A. thaliana*, immunity to *Hpa*  
129 isolate Emwa1 is mediated by RPP4, an NLR that requires EDS1 for function  
130 (20). RPP4-mediated disease resistance was partially compromised in the  
131 *Atmlkl* triple mutant, as measured by increased *Hpa* sporangiophore formation  
132 on true leaves (Fig. 3B). We did not detect marked differences between the  
133 susceptibility of wild-type and mutant plants to hemi-biotrophic *Pseudomonas*  
134 *syringae* pv. *tomato* DC3000 bacteria or the fungal necrotroph *Botrytis cinerea*  
135 (Fig. S5AB). Furthermore, disease resistance mediated by RPS2 and cell  
136 death mediated by RPM1 NLRs were largely retained in the *Atmlkl123* mutant  
137 (Fig. S5CD).

138

139 RNA-seq analysis using mock- and *G. orontii*-challenged leaves of wild-type,  
140 *Atmlkl23*, *Atmlkl123* and *eds1* lines showed that the *AtMLKL1* transcript was  
141 induced upon pathogen challenge (7.4 fold) and that induction was fully  
142 dependent on *EDS1* (Fig. 3C, Fig. S6). Further analysis revealed that  
143 *AtMLKLs* regulate transcriptional reprogramming both under unchallenged  
144 conditions and upon pathogen attack (Fig. 3C). These data imply a specific  
145 and partly redundant role of *AtMLKLs* in resistance to obligate biotrophic  
146 pathogens.

147

148 To test whether *At*MLKLs possess cell death activity, possibly regulated by  
149 phosphorylation, we introduced single phosphomimetic substitutions at serine  
150 residues in the activation loops of *At*MLKLs (Fig. 1B) and expressed in *A.*  
151 *thaliana* leaf protoplasts (see method). Upon overexpression, all wild-type  
152 *At*MLKLs elicited cell death, which was as potent as an N-terminal barley NLR  
153 cell death module (21)(Fig. S7). We found that a phosphomimetic substitution  
154 at serine<sup>393</sup> but not serine<sup>395</sup> in *At*MLKL1 enhanced its cell-killing activity (Fig.  
155 4A). However, an alanine substitution at serine<sup>393</sup> did not compromise the cell  
156 death activity, suggesting that other serine or threonine residues in the  
157 activation loop (Fig. 1B) have a compensatory function. Using transgenic *A.*  
158 *thaliana* lines, we observed that the enhanced susceptibility of *Atmkl1* and  
159 *Atmkl2* mutants to *G. orontii* was restored by stable transformations of  
160 genomic fragments encompassing wild-type *AtMLKL1* and *AtMLKL2*,  
161 respectively (Fig. 4B,C and Fig. S8-9). In line with the protoplast assay (Fig.  
162 4A), *At*MLKL1 (S393D) transgenic plants exhibited enhanced resistance to *G.*  
163 *orontii* compared to Col-0 wild type, plants expressing the transgenes  
164 *At*MLKL1 or *At*MLKL1 (S395D) (Fig. 4B,C). Unexpectedly, *At*MLKL1 (S393D)  
165 transgenic plants did not exhibit cell death lesions or apparent plant growth  
166 retardation indicative of autoimmunity (Fig. 4B, Fig. S8A). Collectively our  
167 results suggest that plant MLKL function is in part regulated by activation loop  
168 conformation, similar to vertebrate MLKLs (22), but *At*MLKL1 activity needed  
169 to restrict *G. orontii* growth can be separated from host cell death.

170

171

172 We next examined whether the *At*MLKL N-terminal HeLo domain contributes  
173 to its cell death activity, as in animals (8, 12, 14, 23). Taking advantage of a  
174 chemically enforced oligomerization system (Fig. S10, see method), we found  
175 that expression of the HeLo domains with the brace region of *At*MLKL1 and  
176 *At*MLKL3 was sufficient for cytotoxic activity and this activity was further  
177 enhanced upon oligomerization (Fig. S10D). This finding mirrors the activity  
178 of the HeLo domains with the brace region of MLKL (14) and is consistent  
179 with our structure-based hypothesis that the full-length MLKL tetramer with  
180 buried HeLo domains represents an inactive form (Fig. 2).

181

182 As animal MLKL translocates to the PM upon activation (10-14) we examined  
183 whether GFP-tagged *At*MLKL variants associate with the PM using time-  
184 resolved confocal microscopy. We detected mobile punctate signals in the  
185 cytoplasmic space for all *At*MLKL1 variants (Fig. 4DE). Reduced mobility for a  
186 fraction of *At*MLKL1-GFP signals when proximal to the PM (Fig. 4E) is  
187 consistent with PM association. Intriguingly, maximum projection of the time-  
188 lapse images revealed that *At*MLKL1 (wild type)-GFP, the S395D mutant  
189 moved along filamentous structures (Fig. 4E, Supplemental movies 1 and 3;  
190 Fig. S11A). These filamentous structures specifically colocalized with the  
191 microtubule marker (24) mCherry-MAP4 (Fig. S11B-C), and association was  
192 detectable upon *G. orontii* invasion (Fig. S12). Intriguingly, no filamentous  
193 structures were detected in the S393D phosphomimetic line despite the  
194 presence of a microtubule array (Fig. S13). These data suggest that specific

195 phosphorylation modulates the intracellular localization and activities of  
196 *AtMLKL1* via cytoskeletal association.

197

198 The plant MLKL family described here is a first example of a non-receptor  
199 immunity component consisting of multiple domains that is structurally shared  
200 between animal and plants. MLKLs in these two kingdoms are likely products  
201 of convergent evolution because their exon-intron structures are unrelated (~4  
202 and 11 exons in *AtMLKLs* and *hMLKL*, respectively). Our work serves as a  
203 template to test structural predictions implicating the presence of a HeLo-  
204 domain fold in a number of plant modular proteins, including the ADR1 family  
205 of NLRs (4, 25-27). Despite the cell death activity of a putative HeLo-domain  
206 of ADR1 (28), this family confers disease resistance without apparent host cell  
207 death (29). This resembles *AtMLKL*-mediated defense in wild-type plants to  
208 *G. orontii* without host cell death, although *AtMLKLs* have the capacity to  
209 elicit cell death. These results raise the question of whether host defence and  
210 cell death functions can be further disentangled in animal necroptosis  
211 signalling.

212

212 **Fig. 1: Plant genomes encode structural homologs of MLKL.**

213 **A**, A diagram of plant and animal MLKLs. A variably sized serine-rich region  
214 that has no similarity to known structures is directly C-terminal to the  
215 pseudokinase domain of plant MLKLs.

216 **B**, Alignments of the four helical bundles (HeLo domain) and the  
217 pseudokinase domains of *A. thaliana* MLKLs (*AtMLKLs*) and representative  
218 vertebrates. Invariant residues and conservative substitutions in > 50% of the  
219 sequences are shown in light blue and grey backgrounds, respectively. The  
220 residues responsible for the activation of human or mouse MLKL upon  
221 phosphorylation are indicated in the red box. The serine residues examined in  
222 this study are shown in red.

223 **C**, Plant MLKL-encoding genes across representative plant species. A full list  
224 of MLKL-encoding genes in the genomes of 48 seed plants is shown in Table  
225 S1.

226 **D**, Phylogenetic relationship of plant MLKLs. Neighbor-net analysis  
227 discriminates two subgroups of plant MLKLs colored in light blue and orange  
228 with bootstrap support of 0.85 (1,000 bootstrap replicates).

229

230 **Fig. 2. Structure of the *AtMLKL3* tetramer.**

231 **A**, Top: Gel filtration profiles of *AtMLKL3*. Position of standard molecular  
232 weight is indicated by arrow. Bottom: Peak fractions on the top were verified  
233 by reducing SDS-PAGE with Coomassie Blue staining.

234

235 **B**, Final EM density map of the *AtMLKL3* tetramer. Local resolution of the  
236 density map is shown on the right with scale indicated by colors, in angstroms.

237

238 **C**, Top: Final 3D reconstruction of *AtMLKL3* tetramer shown in three  
239 orientations. Each monomer of *AtMLKL3* is shown in different colors. Bottom:  
240 Cartoon shows the overall structure of *AtMLKL3* tetramer in three orientations.  
241 Subdomains of *AtMLKL3* are shown in different colors.

242

243 **D** Superposition of the HeLo domains of *AtMLKL3* (yellow, PDB ID code  
244 6KA4), human MLKL (blue, PDB ID code 2MSV) and mouse MLKL (Pink,  
245 PDB ID code 4BTF). RMSD between *AtMLKL3* and mMLKL:3.745, RMSD  
246 between *AtMLKL3* and hMLKL:4.010.

247

248 **E**, Electrostatic surface of HeLo domains of *AtMLKL3*, human MLKL and  
249 mouse MLKL in two orientations.

250

251 **F**, Cartoon shows the brace region of the *AtMLKL3* tetramer. Each monomer  
252 of *AtMLKL3* is shown in different colors.

253 **G**, Cartoon shows the HeLo domains of the *AtMLKL3* tetramer in two  
254 orientations. Each monomer of *AtMLKL3* is shown in different colors.

255

256 **Fig. 3: Arabidopsis MLKLs confer resistance to powdery and downy**  
257 **mildew pathogens.**

258 **A**, *Atmlkl* mutants are susceptible to the powdery mildew *Golovinomyces*  
259 *orontii* (arrowheads). Quantification of *G. orontii* DNA at seven days after  
260 inoculation is relative to the corresponding Col-0 samples. (n=3, Tukey HSD  
261 \**p* < 0.05).

262 **B**, The *Atmlkl* triple mutant is susceptible to the downy mildew  
263 *Hyaloperonospora arabidopsidis*. The number of *Hpa* spores per gram fresh  
264 weight of plants is presented. Data were obtained in three independent  
265 experiments, each including two biological replicates (n=6). Asterisks indicate  
266 significant differences (Tukey HSD *p* < 0.05). The 1<sup>st</sup> or 2<sup>nd</sup> true leaves were  
267 stained with trypan blue to visualise hyphae growth. Sporangioophores were  
268 formed on the true leaves of the *Atmlkl* triple mutant (black arrowheads).

269 **C**, Principal component analysis (PCA) of RNA-seq data from mock- and  
270 pathogen-challenged leaves collected at 48 hours post *G. orontii* inoculation.

271 \*WT is a segregant line derived from the cross between *Atmlkl1* and *Atmlkl3*.  
272 The *eds1* mutant was used as a susceptible control.

273

274 **Fig. 4: Cell death activity, disease resistance and subcellular localization**  
275 **of phosphomimetic AtMLKL1 variants.**

276 **A**, A phosphomimetic substitution in *AtMLKL1* elicited enhanced cell death in  
277 *Arabidopsis* mesophyll protoplasts. Luciferase and *AtMLKL1* expression  
278 constructs were co-transfected into protoplasts and luciferase activity was  
279 measured as a proxy of cell viability at 16 hours post transfection. The  
280 positions of serine-to-aspartate residues are indicated in Fig. 1B. The C-  
281 terminally HA-tagged variants were expressed under the control of the  
282 constitutive cauliflower mosaic virus 35S promoter. (n=3, Tukey HSD \**p* <  
283 0.01).

284 **B**, Macroscopic phenotype of transgenic *Arabidopsis* expressing  
285 phosphomimetic variants of *AtMLKL1* in response to *G. orontii* (arrowheads).  
286 Plants were photographed seven days after pathogen challenge.

287 **C**, Quantification of *G. orontii* DNA in infected leaves of transgenic plants at  
288 14 days after pathogen challenge (n=4, Tukey HSD \**p* < 0.05).

289 **D**, Schematic diagram of the confocal images shown in **B**. The white circle  
290 indicates GFP signal proximal to the PM.

291 **E**, Confocal images of the abaxial epidermis of the *Arabidopsis* transgenic  
292 lines expressing phosphomimetic and wild-type variants of *AtMLKL1*. GFP  
293 signals indicated by white circles were immobile in the examined time period.  
294 The corresponding movies are available as supplemental movies 1-3. The  
295 asterisk indicates plastidial autofluorescence. Scale bars = 5  $\mu$ m.

296

296 **Acknowledgments:** We thank the Max Planck Genome Centre Cologne for  
297 RNA-Seq and Petra Köchner, Sabine Haigis and Makoto Yoshikawa-  
298 Maekawa for technical assistance and Neysan Donnelly for editing the  
299 manuscript. We also thank Hirofumi Nakagami, Ton Timmers, Hamid Kashkar  
300 and Manolis Pasparakis for helpful suggestions. We also thank Takashi  
301 Hashimoto and Stefanie Sprunck for the mcherry-MAP4 and tagRFP-T-Lifeact  
302 vectors, respectively.

303 **Data and materials availability:** All data underlying the study are deposited  
304 at Protein Data bank (PDB): <https://www.rcsb.org/>) or Gene Expression  
305 Omnibus (GEO) database (<https://www.ncbi.nlm.nih.gov/geo/>).

306 **Author contributions:** T.M. conceptualized the project; L.M., M.H., X.Z.,  
307 R.T.N., L.B.K., I.M.L.S., F.J., V.K., D.L., K.H., T.M. performed the  
308 investigations. J.P. J.M.M., P.S-L. J.C. T.M. validated the data, J.P. J.M.M.,  
309 P.S-L. J.C. T.M. supervised the work, J.C. and T.M. wrote the original draft of  
310 the manuscript, J.P. P.S-L., J.M.M. reviewed and edited the manuscript.

311 **Competing interests:** The authors declare no competing interests.

312 **Data and materials availability:** All data needed to replicate the work are  
313 deposited in the Protein Data Bank (PDB) or Gene Expression Omnibus  
314 (GEO) database. Plants and plasmids described in the manuscript are  
315 available upon request.

316



## 316 References

- 317 1. N. S. Coll, P. Epple, J. L. Dangl, Programmed cell death in the plant  
318 immune system. *Cell Death Differ* **18**, 1247-1256 (2011).
- 319 2. W. G. van Doorn, Classes of programmed cell death in plants,  
320 compared to those in animals. *J Exp Bot* **62**, 4749-4761 (2011).
- 321 3. F. K. Chan, N. F. Luz, K. Moriwaki, Programmed necrosis in the cross  
322 talk of cell death and inflammation. *Annu Rev Immunol* **33**, 79-106  
323 (2015).
- 324 4. A. Daskalov *et al.*, Identification of a novel cell death-inducing domain  
325 reveals that fungal amyloid-controlled programmed cell death is related  
326 to necroptosis. *Proc Natl Acad Sci U S A* **113**, 2720-2725 (2016).
- 327 5. L. Sun *et al.*, Mixed lineage kinase domain-like protein mediates  
328 necrosis signaling downstream of RIP3 kinase. *Cell* **148**, 213-227  
329 (2012).
- 330 6. J. Zhao *et al.*, Mixed lineage kinase domain-like is a key receptor  
331 interacting protein 3 downstream component of TNF-induced necrosis.  
332 *Proc Natl Acad Sci U S A* **109**, 5322-5327 (2012).
- 333 7. T. Vanden Berghe, A. Linkermann, S. Jouan-Lanhouet, H. Walczak, P.  
334 Vandenabeele, Regulated necrosis: the expanding network of non-  
335 apoptotic cell death pathways. *Nat Rev Mol Cell Biol* **15**, 135-147  
336 (2014).
- 337 8. E. J. Petrie, P. E. Czabotar, J. M. Murphy, The Structural Basis of  
338 Necroptotic Cell Death Signaling. *Trends Biochem Sci* **44**, 53-63 (2019).
- 339 9. E. J. Petrie, J. M. Hildebrand, J. M. Murphy, Insane in the membrane: a  
340 structural perspective of MLKL function in necroptosis. *Immunol Cell*  
341 *Biol* **95**, 152-159 (2017).
- 342 10. X. Chen *et al.*, Translocation of mixed lineage kinase domain-like  
343 protein to plasma membrane leads to necrotic cell death. *Cell Res* **24**,  
344 105-121 (2014).
- 345 11. Y. Dondelinger *et al.*, MLKL compromises plasma membrane integrity  
346 by binding to phosphatidylinositol phosphates. *Cell Rep* **7**, 971-981  
347 (2014).
- 348 12. J. M. Hildebrand *et al.*, Activation of the pseudokinase MLKL unleashes  
349 the four-helix bundle domain to induce membrane localization and  
350 necroptotic cell death. *Proc Natl Acad Sci U S A* **111**, 15072-15077  
351 (2014).
- 352 13. H. Wang *et al.*, Mixed lineage kinase domain-like protein MLKL causes  
353 necrotic membrane disruption upon phosphorylation by RIP3. *Mol Cell*  
354 **54**, 133-146 (2014).
- 355 14. G. Quarato *et al.*, Sequential Engagement of Distinct MLKL  
356 Phosphatidylinositol-Binding Sites Executes Necroptosis. *Mol Cell* **61**,  
357 589-601 (2016).
- 358 15. A. Bendahmane, K. Kanyuka, D. C. Baulcombe, The Rx gene from  
359 potato controls separate virus resistance and cell death responses.  
360 *Plant Cell* **11**, 781-792 (1999).
- 361 16. N. S. Coll *et al.*, Arabidopsis type I metacaspases control cell death.  
362 *Science* **330**, 1393-1397 (2010).
- 363 17. J. S. Pearson, J. M. Murphy, Down the rabbit hole: Is necroptosis truly  
364 an innate response to infection? *Cell Microbiol* **19**, (2017).

- 365 18. G. Manning, D. B. Whyte, R. Martinez, T. Hunter, S. Sudarsanam, The  
366 protein kinase complement of the human genome. *Science* **298**, 1912-  
367 1934 (2002).
- 368 19. W. Wang, Y. Wen, R. Berkey, S. Xiao, Specific targeting of the  
369 Arabidopsis resistance protein RPW8.2 to the interfacial membrane  
370 encasing the fungal Haustorium renders broad-spectrum resistance to  
371 powdery mildew. *Plant Cell* **21**, 2898-2913 (2009).
- 372 20. E. A. van der Biezen, C. T. Freddie, K. Kahn, J. E. Parker, J. D. Jones,  
373 Arabidopsis RPP4 is a member of the RPP5 multigene family of TIR-  
374 NB-LRR genes and confers downy mildew resistance through multiple  
375 signalling components. *Plant J* **29**, 439-451 (2002).
- 376 21. F. Jacob *et al.*, A dominant-interfering camta3 mutation compromises  
377 primary transcriptional outputs mediated by both cell surface and  
378 intracellular immune receptors in Arabidopsis thaliana. *New Phytol* **217**,  
379 1667-1680 (2018).
- 380 22. J. M. Murphy *et al.*, The pseudokinase MLKL mediates necroptosis via  
381 a molecular switch mechanism. *Immunity* **39**, 443-453 (2013).
- 382 23. M. C. Tanzer *et al.*, Evolutionary divergence of the necroptosis effector  
383 MLKL. *Cell Death Differ* **23**, 1185-1197 (2016).
- 384 24. J. Marc *et al.*, A GFP-MAP4 reporter gene for visualizing cortical  
385 microtubule rearrangements in living epidermal cells. *Plant Cell* **10**,  
386 1927-1940 (1998).
- 387 25. A. R. Bentham, R. Zdrzalek, J. C. De la Concepcion, M. J. Banfield,  
388 Uncoiling CNLs: Structure/Function Approaches to Understanding CC  
389 Domain Function in Plant NLRs. *Plant Cell Physiol* **59**, 2398-2408  
390 (2018).
- 391 26. C. Barragan *et al.*, RPW8/HR Repeats Predict NLR-dependent Hybrid  
392 Performance. *bioRxiv*, 559864 (2019).
- 393 27. L. M. Jubic, S. Saile, O. J. Furzer, F. El Kasmi, J. L. Dangl, Help  
394 wanted: helper NLRs and plant immune responses. *Curr Opin Plant*  
395 *Biol* **50**, 82-94 (2019).
- 396 28. S. M. Collier, L. P. Hamel, P. Moffett, Cell death mediated by the N-  
397 terminal domains of a unique and highly conserved class of NB-LRR  
398 protein. *Mol Plant Microbe Interact* **24**, 918-931 (2011).
- 399 29. V. Bonardi *et al.*, Expanded functions for a family of plant intracellular  
400 immune receptors beyond specific recognition of pathogen effectors.  
401 *Proc Natl Acad Sci U S A* **108**, 16463-16468 (2011).

402

## 402 **Methods**

### 403 **Plant material and growth conditions**

404 *The Arabidopsis thaliana* (L.) Heynh. ecotype Columbia (Col-0) was used in  
405 this study. The T-DNA insertional mutants(1, 2) (SALK\_041569c (*AtMLKL1*),  
406 SALK\_124412c (*AtMLKL2*) and GABI\_491E02 (*AtMLKL3*) were obtained  
407 from the Nottingham Arabidopsis Stock Centre (NASC). Double and triple  
408 mutants of *Atmkl* were generated by crossing the T-DNA insertion lines. A  
409 segregant line derived from the cross between the *Atmkl1* and *Atmkl3*  
410 mutants were used as a wild-type line in addition to Col-0 wild-type. Each  
411 genotype was confirmed by PCR. The *eds1-2* mutant was described  
412 previously (3).

413 *The transgenic lines expressing AtMLKL1 variants or AtMLKL2 fused to a*  
414 *monomeric green fluorescence protein* were established in *Atmkl1* and  
415 *Atmkl2* mutant backgrounds, respectively. Genomic fragments including  
416 coding region and native *cis*-regulatory sequence were amplified by PCR from  
417 Col-0 genomic DNA and cloned into pENTR/D-TOPO (Thermo Fisher  
418 Scientific, Waltham, MA, USA). The phosphomimetic substitutions were  
419 introduced using the QuikChange Lightning site-directed mutagenesis kit  
420 (Agilent Technologies, Santa Clara, CA, USA). Resulting entry vectors were  
421 transferred into pGWB550(4) using LR clonase II (Thermo Fisher Scientific).  
422 Plants were transformed by the floral dip method (5) with *Agrobacterium*  
423 *tumefaciens* strain GV3101 harbouring pMP90RK (6). Plant growth conditions  
424 were described previously (7). Primer sequences for genotyping and plasmid  
425 construction are listed in Table S3.

426

## 427 **Sequence analysis of plant and animal MLKLs**

428 Sequence similarity within the animal and plant families was established by  
429 the generalized profile method (8). Sequences were aligned by the L-INS-I  
430 method of the MAFFT alignment software (9), followed by minor manual  
431 editing of ambiguously aligned regions. Sequence similarity between the  
432 animal and plant MLKL families was established by Hidden Markov Model  
433 (HMM)-to-HMM comparison using the HHSEARCH package (10). The 99,696  
434 orthogroups (OGs) among 52 plant species have been established recently  
435 (11). An OG containing *At*MLKLs was used for the neighbor-net analysis of  
436 codon-aligned nucleotide sequence as described previously (12). The  
437 sequence from the papaya genome was excluded in this study.

## 438 **Protein expression and purification**

439 Full length *At*MLKL3 (residues 1-701) with an engineered C-terminal 6×His  
440 tag was generated by standard PCR-based cloning strategy and its identity  
441 was confirmed by sequencing. The protein was expressed in sf21 insect cells  
442 using the vector pFastBac 1 (Invitrogen). One litre of cells ( $2.5 \times 10^6$  cells ml<sup>-1</sup>,  
443 medium from Expression Systems) was infected with 20 ml baculovirus at  
444 28°C. After growth at 28°C for 48 hours, the cells were harvested, re-  
445 suspended in the buffer containing 50 mM Tris-HCl pH 8.0 and 300 mM NaCl,  
446 and lysed by sonication. The soluble fraction was purified from the cell lysate  
447 using Ni<sup>2+</sup>-nitrilotriacetate affinity resin (Ni-NTA, Qiagen). The protein was  
448 then further purified by further purified by gel filtration (Superose 6, 10/30; GE  
449 Healthcare). For cryo-EM investigation, the purified protein was concentrated  
450 to about 0.3 mg/mL in buffer containing 50 mM Tris-HCl pH 8.0, 300 mM NaCl  
451 and 3 mM DTT.

452 The construct of full length *Af*MLKL2 (residues 1-711) with N-terminal GST  
453 tag was cloned into the pGEX-6P-1 vector (GE Healthcare), and was  
454 expressed in *Escherichia coli* strain BL21(DE3; Novagen) at 16 °C. After  
455 isopropyl- $\beta$ -D-thiogalactopyranoside (IPTG; Sigma) induction for 12 h, cells  
456 were harvested and re-suspended in buffer containing 50 mM Tris-HCl pH 8.0  
457 and 300 mM NaCl, and lysed by sonication. The soluble fraction was purified  
458 from the cell lysate using Glutathione Sepharose 4B beads (Invitrogen). The  
459 proteins were then digested with PreScission protease (GE Healthcare) to  
460 remove the GST tag and further purified by gel filtration (Superose 6, 10/30;  
461 GE Healthcare). For cryo-EM investigation, the purified protein was  
462 concentrated to about 0.3 mg/mL in buffer containing 50 mM Tris-HCl pH 8.0,  
463 300 mM NaCl and 3 mM DTT.

#### 464 **Cryo-EM sample preparation and data collection**

465 For cryo-EM analysis, an aliquot of 3.5  $\mu$ l *Af*MLKL2 or *Af*MLKL3 protein was  
466 applied to a holey carbon grids (Quantifoil Cu 1.2/1.3, 200 mesh) glow-  
467 discharged (Harrick Plasma) with a middle force for 30 s after evaluating for 2  
468 min. The grids were blotted by a pair of 55 mm filter papers (TED PELLA,  
469 INC.) for 3-3.5 s at 8 °C with 100% humidity and flash-frozen in liquid ethane  
470 using a FEI Vitrobot Marked IV. Cryo-EM data were collected on Titan Krios  
471 electron microscope operated at 300 kV and a Gatan K2 Summit direct  
472 electron detection camera (Gatan) using eTas. Micrographs were recorded in  
473 super-resolution mode at a nominal magnification of 22500  $\times$ , resulting in a  
474 physical pixel size of 1.30654 Å per pixel. Defocus values varied from -1.7  $\mu$ m  
475 to -2.3  $\mu$ m for data set. The dose rate was 10.6 electron per pixel per second.

476 Exposures of 8.0 s were dose-fractionated into 32 sub-frames, leading to a  
477 total accumulated dose of 50 electrons per Å<sup>2</sup>. In total, two batches of data  
478 were collected, one for AtMLKL3 and another for AtMLKL2.

#### 479 **Image processing and 3D reconstruction**

480 A total of 1,434 and 1,828 raw images stacks of AtMLKL3 and AtMLKL2  
481 acquired under super-resolution mode, were 2x binned processed using  
482 MotionCor2 (13), generating aligned, dose-weighted and summed  
483 micrographs in a pixel size of 1.30654 Å per pixel. CTFFIND4 (14) was used  
484 to estimate the contrast transfer function (CTF) parameters. After the removal  
485 of bad micrographs via the evaluation of CTF parameters, remaining images  
486 were processed in RELION (15). Approximate 2,000 particles were manually  
487 picked and 2D-classified to generate templates for auto-picking. 983,779 and  
488 1,135,463 autopicked particles for AtMLKL3 and AtMLKL2 respectively were  
489 then used for reference-free 2D classification, to remove contaminants and  
490 bad particles. The left good particles were subjected to 3D classification using  
491 initial 3D reference model obtained by *ab initio* calculation from Relion3.0.  
492 Particles from good classes that possess density map with better overall  
493 structure features were selected for the 3D refinement. The final 3D  
494 refinement using D2 symmetry resulted in reconstructions of AtMLKL3 and  
495 AtMLKL2 tetramer at resolution of 3.4 Å and 4.1 Å, the resolutions were  
496 determined by gold-standard Fourier shell correlation. Local resolution  
497 distribution was evaluated using Relion.

498

499

## 500 **Model building and refinement**

501 EM density map of *At*MLKL3 was used to build the model de novo, as the  
502 overall resolution of map density was efficient to display side chains. The  
503 model of *At*MLKL3 was manually built into the density in COOT(16), and was  
504 refined against the EM map by PHENIX(17) in real space with secondary  
505 structure and geometry restraints. The refined *At*MLKL3 model was docked  
506 into the density of *At*MLKL2. The sequence of the docked *At*MLKL3 model  
507 was changed to that of *At*MLKL2 under COOT and the *At*MLKL2 model with  
508 corrected sequence was subjected to refinement by PHENIX. The C-terminal  
509 serine-rich region of *At*MLKL2 or *At*MLKL3 is much less well defined in the  
510 density and is not included in the models. Final model of *At*MLKL3 and  
511 *At*MLKL2 was validated using MolProbity and EMRinger in PHENIX package.  
512 The structures of human MLKL (18) and mouse MLKL (19) were used for the  
513 superposition of the HeLo domains as shown in Fig. 2D. Table S2 summarized  
514 the model statistics.

## 515 **RNA sequencing**

516 Total mRNA from leaves was obtained at 48 hours after challenge with  
517 conidia of *Golovinomyces orontii* using the RNeasy plant mini kit (Qiagen).  
518 RNA sequencing (RNA-Seq) libraries were prepared by the Max Planck  
519 Genome Centre Cologne (Cologne, Germany) using the Illumina TruSeq  
520 stranded RNA sample preparation kit (Illumina). The resulting libraries were  
521 subjected to 150-bp single-end sequencing using the Illumina HiSeq3000  
522 (Illumina). Mapping of sequenced reads onto the *Arabidopsis thaliana* gene  
523 model (TAIR10), principal component analysis, and differential gene  
524 expression analysis were performed in the CLC Genomics Workbench



525 (Qiagen, ver. 10.1.2) using the tool 'RNA-Seq with the default parameter  
526 setting. The data derived from Col-0 and WT were pooled as data of wild-type  
527 lines in the analysis. The heat map of 93 genes differentially expressed  
528 between wild type lines and *Atmkl* mutants ( $|\log_2FC| > 1$  and false discovery  
529 rate (FDR)  $< 0.05$ ) were generated using the R package (ver. 1.08) with the  
530 pheatmap function. Gene ontology enrichment analysis was performed using  
531 the PANTHER classification system (<http://pantherdb.org/>) with default  
532 settings for *Arabidopsis thaliana*. The RNA-Seq data generated in this study  
533 have been deposited in the Gene Expression Omnibus (GEO) database  
534 under accession number GSE129011.

535

### 536 **Transient gene expression in *Arabidopsis* protoplasts**

537 Isolation, transfection and luciferase activity measurement of *Arabidopsis*  
538 protoplasts were performed as described previously (20). Protoplasts were  
539 isolated from the leaves of two-week-old *Arabidopsis* plants grown in liquid 1 x  
540 Murashige and Skoog medium. Coding sequences (CDS) of *AtMLKL1* and  
541 *AtMLKL2* without stop codons were initially cloned into pENTR/D-TOPO  
542 (Thermo Fisher Scientific). The CDS of *AtMLKL3* without a stop codon was  
543 chemically synthesized and cloned into pENTR221 (Thermo Fisher Scientific).  
544 Two synonymous substitutions (G1371T and A1413G) were introduced into  
545 *AtMLKL3* CDS to remove restriction sites that hamper the DNA synthesis.  
546 Entry clones were transferred into the gateway cloning-compatible pAMPAT-  
547 GW-mYFP, pAMPAT-GW-3xHA, or pAMPAT-GW expression vectors (21),  
548 which are derivatives of pAMPAT-MCS (accession number: AY436765).  
549 Primers sequences of for plasmid construction are listed in Table S3. pENTR-



550 tagRFP-T-Lifeact (22) was transferred into pAMPAT-GW. The expression  
551 vectors for *HvMLA*(1-160aa), MAP4 and Tub6 were described previously (21,  
552 23, 24).

### 553 **Protoplast viability assay**

554 Following protoplast transfection and regeneration, Evans blue dye dissolved  
555 in water was added to the samples to a final concentration of 0.04% (w/v).  
556 The stained cells were examined under a standard microscope. For  
557 luciferase-based viability assay luciferase and *AfMLKL* expression constructs  
558 were co-transfected into protoplasts and luciferase activity was measured as  
559 a proxy of cell viability.

560

### 561 **Induced oligomerization**

562 Two domains of FKBP (F36V) tagged with HA without N-myristoylation signal  
563 were PCR amplified from pC4M-FV2E plasmid (ARIAD, Cambridge, MA,  
564 USA). *NcoI* and *HindIII* restriction sites were added to the 5' end of forward  
565 and reverse primers, respectively. The digested PCR fragment with *NcoI* and  
566 *HindIII* were ligated into the same restriction sites present between the attR2  
567 and the terminator sequences of pAMPAT-GW expression vector. The  
568 resulting vector is named pAMPAT-GW-FV2E-HA. Coding regions  
569 corresponding to the N- and C-terminal luciferase fragments (nLUC and  
570 cLUC) were PCR amplified from nLUC and cLUC expression vectors (25) and  
571 cloned into pENTR/D-TOPO. Respective entry clones were transferred into  
572 pAMPAT-GW-FV2E-HA. B/B homodimerizer (also known as AP20187 ligand)  
573 were purchased from TakaraBio, Japan. After transfection, protoplasts in

574 incubation buffer (i.e. WI solution (26)) were separated into two tubes and  
575 added the same amount of incubation buffer supplemented with B/B  
576 homodimerizer (250 nM at the final concentration) or ethanol as solvent  
577 control. Primer sequences for the plasmid construction are listed in Table S2.  
578 We were able to reconstitute luciferase activity of co-expressed N- and C-  
579 terminal halves of luciferase fused to 2xDmrB domains in a ligand-specific  
580 manner (Fig. S8b) and the ligand itself did not affect the luciferase reporter  
581 assay in protoplasts (Fig. S8c).

### 582 **Pathogen infection assay**

583 The *G. orontii* infection assay was performed as described previously (27). *G.*  
584 *orontii* DNA was quantified by qPCR at indicated time points after inoculation  
585 of conidia and normalised using the amount of plant specific gene  
586 (AT3G21215). The *Hpa* infection assay was performed as previously  
587 described (28). Lactophenol-trypan blue staining was described previously  
588 (29). The *B. cinerea* strain B05.10 was used in this study. Droplet inoculation  
589 of six-week-old plants was performed as described previously (30), except  
590 that 2 µl of the spore solution were used on each side of the leaf and two  
591 leaves of similar age were used per plant. *B. cinerea* DNA was quantified by  
592 qPCR as previously described (31). *Pseudomonas syringae* pv. *tomato* (*Pst*)  
593 DC3000 and *Pst* DC3000 expressing *AvrRpt2* or *AvrRpm1* were used in this  
594 study. *Pst* growth assays and ion leakage measurement following bacterial  
595 infiltration were performed as described previously (7).

596

597

598 **Immunoblot assays**

599 Primary antibodies were monoclonal antibodies from mouse:  $\alpha$ -GFP (JL-8,  
600 1:5000, Takara, Shiga, Japan) or rat:  $\alpha$ -HA (3F10, 1:1000, Sigma-Aldrich, St.  
601 Louis, MO, USA). Goat  $\alpha$ -mouse IgG-HRP (1:10000, Santa Cruz  
602 Biotechnology, Dallas, TX, USA) or goat  $\alpha$ -rat IgG-HRP (1:10000, Sigma-  
603 Aldrich) were used as secondary antibodies. The detailed procedure is  
604 described in (7).

605

606 **Biolistic transient gene expression**

607 Biolistic delivery of plasmid DNA into the abaxial epidermis of leaves was  
608 essentially performed as described previously (32). Leaves were detached  
609 immediately before bombardment and the bombarded leaves were transferred  
610 to 1% agar plates supplemented with 85  $\mu$ M benzimidazole and incubated at  
611 20°C for 15 h before confocal microscopy.

612

613 **Confocal microscopy**

614 Transfected protoplasts in a chamber slide (Nunc Lab-Tek, Thermo Fisher  
615 Scientific) with incubation buffer (i.e. WI solution, (26)) or 2-5 mm leaf discs  
616 prepared from rosette leaves of 4-5-week-old plants were observed under a  
617 confocal microscope (LSM880, Carl Zeiss) equipped with a 40X water-  
618 immersion and a 63X oil-immersion objective. Lambda stack images were  
619 obtained for spectral imaging. Images were analyzed and processed with ZEN  
620 Software (Carl Zeiss) and ImageJ (NIH). In Fig. 4E, confocal images were  
621 acquired over time (for wild type, 124 seconds; for S393D, 194 seconds; for

622 S395D, 166 seconds) and used for maximum intensity projection (bottom  
623 panels). Representative single frame images are shown (top panels).

624

624 **Supplemental data**

625 **Supplemental Fig. 1: 3D reconstruction of *At*MLKL3 tetramer**

626 **A**, Representative cryo-EM image of *At*MLKL3 tetramer. Representative  
627 particles are indicated with black circles.

628 **B**, Representative top and side views of 2D class averages of *At*MLKL3  
629 tetramer.

630 **C**, Fourier shell correlation (FSC) curves at 0.5 and 0.143 of the 3D  
631 reconstruction of *At*MLKL3 tetramer.

632 **D**, Flowchart representing cryo-EM data processing and 3D reconstruction of  
633 *At*MLKL3 tetramer.

634

635 **Supplemental Fig. 2: Purification and 3D reconstruction of *At*MLKL2  
636 tetramer**

637 **A**, Top: Gel filtration profile of *At*MLKL2 protein. Position of standard  
638 molecular weight is indicated by arrow. Bottom: Peak fractions in the top were  
639 verified by SDS-PAGE with Coomassie Blue staining.

640 **B**, Representative cryo-EM images of the *At*MLKL2 tetramer. Representative  
641 particles are indicated with black circles.

642 **C**, Representative top and side views of 2D class averages of *At*MLKL2  
643 tetramer.

644 **D**, Fourier shell correlation (FSC) curves at 0.5 and 0.143 of the 3D  
645 reconstruction of *At*MLKL2 tetramer.

646 **E**, Flowchart representing cryo-EM data processing and 3D reconstruction of  
647 *At*MLKL2 tetramer.

648

649 **Supplemental Fig. 3: Inter- and intra-domain interactions of *At*MLKL3  
650 tetramer and structural comparison of the *At*MLKL2 and *At*MLKL3**

651 **A**, Superposition of *At*MLKL2 (grey) and *At*MLKL3 (blue). RMSD between  
652 monomer of *At*MLKL2 and *At*MLKL3 :0.985.

653 **B**, The sequence of *At*MLKL3 model (blue) was docked into *At*MLKL2 map  
654 (gray).

655

656 **C**, Top: Cartoon representation of *At*MLKL3 monomer in two orientations.  
657 Subdomains of *At*MLKL3 are shown in different colors, the interacting regions  
658 between domains are highlighted with open frames. Bottom left: Detailed  
659 interactions of HeLo domain and pseudokinase domain for the red-framed  
660 region. Bottom right: Detailed interactions of HeLo domain and brace region  
661 for the blue-framed region.

662

663 **D**, Structural comparison of the monomer *At*MLKL2 (left), *At*MLKL3 (middle,  
664 PDB ID code 6KA4) and *m*MLKL (right, PDB ID code 4BTF).

665

666 **E**, Top left: Cartoon showing HeLo domain and brace region of *At*MLKL3  
667 tetramer. Top right: Detailed interactions of HeLo domains for the green-

668 framed region. Bottom left: Detailed C-terminal interactions of brace regions  
669 for the blue-framed region. Bottom right: Detailed N-terminal interactions of  
670 brace regions for the blue-framed region.

671

672 **Supplemental Fig. 4: *Atmlkl* mutants exhibit no obvious growth defect.**

673 **A**, The Arabidopsis *MLKL* genes and T-DNA insertion sites of the *Atmlkl*  
674 mutants. White and black boxes indicate non-coding and coding exons,  
675 respectively. A gene model for *AtMLKL3* was deduced from other plant *MLKL*  
676 structures.

677 **B**, Representative images of four-week-old plants of Col-0, wild type\*, single  
678 mutants of *Atmlkl1*, *Atmlkl2*, *Atmlkl3*, double mutants *Atmlkl1 2*, *Atmlkl1 3*,  
679 *Atmlkl2 3*, and the triple mutant *Atmlkl1 2 3*. \*The wild type is a segregant line  
680 derived from the cross between *Atmlkl1* and *Atmlkl3*. The plants were initially  
681 grown on Murashige and Skoog-agar plates for two weeks and subsequently  
682 transferred to Jiffy pots rehydrated in water with a fertilizer. Plants were grown  
683 for an additional two weeks under short-day conditions.

684

685 **Supplemental Fig. 5: Arabidopsis MLKLs do not confer resistance to**  
686 ***Botrytis cinerea* and *Pseudomonas syringae* DC3000.**

687 **A**, *Botrytis cinerea* DNA was quantified by qPCR at three days after spore  
688 inoculation and normalized using the amount of plant specific gene (see  
689 method). Amounts are presented relative to the corresponding Col-0 samples.  
690 The wild type is a segregant line derived from the cross between *Atmlkl1* and  
691 *Atmlkl3* (see Fig. S4). Data were obtained in three independent experiments  
692 (n=3).

693 **B**, Log<sub>10</sub>-transformed colony forming units of *Pseudomonas syringae* DC3000  
694 per cm<sup>2</sup> of *A. thaliana* leaves at two days after pathogen infiltration. The *eds1*  
695 mutant was used as a susceptible control. Data were obtained in three  
696 independent experiments (n=3).

697 **C**, Log<sub>10</sub>-transformed colony forming units of *P. syringae* DC3000 expressing  
698 AvrRpt2 per cm<sup>2</sup> of *A. thaliana* leaves at three days after pathogen infiltration.  
699 The *rpm1 rps2* mutant was used as a susceptible control. Data were obtained  
700 in three independent experiments (n=3).

701 **D**, Ion leakage assay in *A. thaliana* leaves upon infiltration with *P. syringae*  
702 DC3000 expressing AvrRpm1. Samples were collected 30 min post infiltration  
703 with the bacterial suspension (OD<sub>600</sub>=0.1). The *rpm1 rps2* mutant was used  
704 as a negative control. Data were obtained in three independent experiments  
705 (n=3).

706 n.s. not significant.

707 **Supplemental Fig. 6: Heat map of 93 genes differentially expressed in**  
708 ***Atmlkl123* in comparison to wild type.** The gene ontology (GO) term biotic  
709 or abiotic stresses (GO:0006950, asterisks) was overrepresented in the down-  
710 regulated transcripts in *Atmlkl123* compared to wild type lines. Mock- and

711 pathogen-challenged leaves were collected at 48 hours post *G. orontii*  
712 inoculation. \*WT is a segregant line derived from the cross between *Atmlk1*  
713 and *Atmlk3*.

714 **Supplemental Fig. 7: AtMLKLs are capable of eliciting cell death in**  
715 ***Arabidopsis* mesophyll protoplasts.**

716 **A**, C-terminally HA-tagged and **B**, C-terminally mYFP-tagged AtMLKLs were  
717 expressed under the constitutive cauliflower mosaic virus 35S promoter.  
718 Expression constructs for AtMLKLs were transfected into protoplasts and cells  
719 were stained with Evans blue at 16 hours post transfection. Unstained cells  
720 (Evans blue-negative cells) were counted as living cells. For **B**, The N-  
721 terminal signalling region of barley NLR protein (*HvMLA<sub>1-160</sub>*: (7) was used as  
722 a positive control. Data were obtained in three independent transfections  
723 (n=3) and different letters indicate statistically significant differences (Tukey  
724 HSD,  $p < 0.01$ ).

725 **C**. Phosphomimetic substitutions in AtMLKL2 or AtMLKL3 do not alter cell  
726 death in *Arabidopsis* mesophyll protoplasts.

727 Expression constructs for luciferase and each of the AtMLKL variants were  
728 co-transfected into protoplasts and luciferase activity was measured as a  
729 proxy for cell viability at 16 hours post transfection. The positions of serine-to-  
730 aspartate substitutions are indicated in Fig. 1B. The C-terminally HA-tagged  
731 variants were expressed under the 35S promoter. Data were obtained in three  
732 independent transfections (n=3). n.s. not significant.

733 **D**, Western blot analysis of expression of C-terminally HA-tagged AtMLKLs in  
734 *Arabidopsis* mesophyll protoplasts. Total protein extracts were collected at  
735 seven hours post transfection. Samples that were transfected with the  
736 corresponding empty vector or the expression construct for AtMLKL2-mYFP  
737 were used as negative control.

738

739 **Supplemental Fig. 8: Genetic complementation of the *Atmlk1* mutant.**

740 **A**, Macroscopic phenotype of transgenic *Arabidopsis* lines expressing wild-  
741 type or phosphomimetic variants of AtMLKL1-GFP under the native *cis*-  
742 regulatory sequence in *Atmlk1* in response to *G. orontii*. Plants were  
743 photographed seven days after pathogen challenge.

744 **B**, Western blot analysis of the C-terminally GFP-tagged AtMLKL1 variants in  
745 the stable transgenic lines. Total protein extracts were collected from two-  
746 week-old plants of the transgenic lines grown on sterile Murashige and Skoog  
747 solid media.

748

749 **Supplemental Fig. 9: Genetic complementation of the *Atmlk2* mutant.**

750 **A**, Macroscopic phenotype of transgenic *Arabidopsis* lines expressing  
751 AtMLKL2-GFP under the native *cis*-regulatory sequence in *Atmlk2*. Four-



752 week-old plants were inoculated with *G. orontii* spores and plants were  
753 photographed at 14 days after pathogen challenge.

754 **B**, Western blot analysis of C-terminally GFP-tagged *AtMLKL2*. Total protein  
755 extracts were collected from two-week-old plants of the transgenic lines grown  
756 on sterile Murashige and Skoog solid media.

757 The asterisk and arrow indicate non-specific and specific bands, respectively.

758 **C**, Quantification of *G. orontii* DNA in infected leaves. Four-week-old plants  
759 were inoculated with spores of the powdery mildew and plants were examined  
760 at 14 days after the pathogen challenge. Fungal DNA was quantified by qPCR  
761 and normalised using the amount of plant specific gene (*AT3G21215*). The  
762 relative amounts to corresponding Col-0 wild-type samples were presented.  
763 Experiments were repeated three times ( $n=3$ ) and the asterisk indicates a  
764 statistically significant difference (Tukey HSD,  $p < 0.05$ ).

765

766 **Supplemental Fig. 10: N-terminal domains of *AtMLKL1* and 3 were**  
767 **sufficient to elicit cell death and their enforced oligomerization**  
768 **potentiated the activities.**

769 **A**, Schematic of chemically induced oligomerization. AP20187 (Dimerizer), a  
770 synthetic cell-permeable ligand, induces homodimerization of fusion proteins  
771 containing the DmrB domain. Dimerizer-dependent oligomerization is  
772 facilitated by a tandem fusion of DmrB domains.

773 **B**, Dimerizer-induced reconstitution of luciferase activity of the N- or C-  
774 terminal halves of luciferase fused with 2 x DmrB domains. Data were  
775 obtained with eight independent transfections ( $n=8$ ). Luciferase activity was  
776 measured at 16 hours post transfection. The luciferase activity was  
777 statistically higher in the presence of dimerizer (one sample *t*-test,  $p < 0.01$ ).

778 **C**, Dimerizer does not influence the luciferase reporter assay. Data were  
779 obtained with seven independent transfections ( $n=7$ ). Luciferase activity was  
780 measured at 16 hours post transfection. No statistically significant differences  
781 were detected (one sample *t*-test).

782 **D**, HeLo domain plus brace region of *AtMLKL1* and *AtMLKL3* were sufficient  
783 to elicit cell death and their enforced oligomerization potentiated the activities.  
784 Expression constructs for luciferase and each of the *AtMLKL* fusion proteins  
785 indicated in the figure were co-transfected into protoplasts and luciferase  
786 activity was measured as a proxy of cell viability at 16 hours post transfection.  
787 Relative luciferase activities compared to those of the empty vector control  
788 with dimerizer were plotted. Data were obtained with eight independent  
789 transfections ( $n=9$ ). Asterisks indicate statistically significant differences  
790 (Tukey HSD,  $p < 0.01$ )

791 **E**, Western blot analysis of the HeLo domain plus brace region constructs  
792 expressed in *Arabidopsis* mesophyll protoplasts. The fusion proteins were  
793 expressed as C-terminally HA-tagged proteins. Total protein extracts were  
794 collected at seven hours post-transfection.



795 **B-E**, Mesophyll protoplasts were prepared from the triple mutant *Atmkl123*  
796 and AP20187 (Dimerizer) was added after transfection (see method).

797

798 **Supplemental Fig. 11: Subcellular localization of AtMLKLs in protoplasts.**

799 **A**, Subcellular localization of AtMLKLs in *Arabidopsis* mesophyll protoplasts.  
800 The C-terminally monomeric YFP (mYFP)-tagged variants were expressed  
801 under the 35S promoter. Representative confocal images were taken at ten  
802 hours post transfection. Scale bars = 10  $\mu$  m.

803 **B**, Co-expression of AtMLKL1 and cytoskeleton markers in *Arabidopsis*  
804 mesophyll protoplasts. Co-expression of AtMLKL1-mYFP and mcherry-MAP4  
805 (microtubule marker: (33) top panels), or tagRFP-T-Lifeact (Actin marker: (34)  
806 middle panels). Representative confocal images were taken at 10 hours post  
807 transfection. Scale bars = 10  $\mu$  m.

808 **C**, The filamentous structures of AtMLKL1-mYFP were undetectable at 5  
809 minutes after application of 5  $\mu$ M of the microtubule inhibitor, oryzalin.  
810 Representative confocal image was taken at 10 hours post transfection.  
811 Scale bar = 10  $\mu$  m.

812 **Supplemental Fig. 12: Confocal images of an epidermal cell that was**  
813 **infected by *G. orontii***. The maximum intensity projection was obtained from  
814 confocal Z-stack images and the autofluorescence of fungal structures were  
815 discriminated from AtMLKL1-GFP signals by spectral imaging. Arrowheads  
816 indicate filamentous structures associated with AtMLKL1-GFP. C; cytoplasm,  
817 Ha: haustorium, E, haustorial encasement. Scale bar = 5  $\mu$ m.

818 **Supplemental Fig. 13: Cortical microtubule arrays in abaxial leaf**  
819 **epidermal cells of transgenic *A. thaliana* lines expressing**  
820 **phosphomimetic and wild type variants of AtMLKL1**. Representative  
821 images were obtained one day after biolistic delivery of the expression  
822 construct for the Atubiquitin10 promoter driven by mCherry-TUB6 (microtubule  
823 marker (24)) into the indicated transgenic lines. Scale bars = 10  $\mu$  m.

824

825 **Supplemental movie 1**

826 Dynamics of AtMLKL1(wild-type)-GFP in a non-pathogen-challenged abaxial  
827 leaf epidermal cell. The corresponding projection image is shown in Fig. 4E.  
828 The white circle indicates a GFP signal proximal to the PM (see Fig. 4D) and  
829 which was less mobile compared to other signals.

830

831 **Supplemental movie 2**

832 Dynamics of AtMLKL1(S393D)-GFP in a non-pathogen-challenged abaxial  
833 leaf epidermal cell. The corresponding projection image is shown in Fig. 4E.

834 The white circle indicates a GFP signal proximal to the PM (see Fig. 4D) and  
835 which was less mobile compared to other signals.

836

837 **Supplemental movie 3**

838 Dynamics of *AtMLKL1*(S395D)-GFP in a non-pathogen-challenged abaxial  
839 leaf epidermal cell. The corresponding projection image is shown in Fig. 4E.  
840 The white circle indicates a GFP signal proximal to the PM (see Fig. 4D) and  
841 which was less mobile compared to other signals.

842

843 **Supplemental file 1**

844 108 coding sequences (CDS) of plant *MLKLs* belong to the same orthogroups  
845 (11). A CDS derived from *Arabidopsis halleri* is incomplete due to the  
846 ambiguous assembly of the corresponding genomic region.

847

847

**Table S1. Number of MLKL-like genes in plant genomes**

Plant species	NCBI Taxonomy ID	Family	Number of <i>MLKL</i> -like genes
<i>Coccomyxa subellipsoidea</i>	248742	Coccomyxaceae	0
<i>Ostreococcus lucimarinus</i>	242159	Bathycoccaceae	0
<i>Volvox carteri</i>	3067	Volvocaceae	0
<i>Physcomitrella patens</i>	3218	Funariaceae	0
<i>Selaginella moellendorffii</i>	88036	Selaginellaceae	0
<i>Actinidia chinensis</i>	3625	Actinidiaceae	3
<i>Amborella trichopoda</i>	13333	Amborellaceae	1
<i>Spirodela polyrhiza</i>	29656	Araceae	2
<i>Phoenix dactylifera</i>	42345	Arecaceae	3
<i>Arabidopsis halleri</i>	81970	Brassicaceae	2
<i>Arabidopsis lyrata</i>	59689	Brassicaceae	3
<i>Arabidopsis thaliana</i>	3702	Brassicaceae	2
<i>Brassica oleracea</i>	3712	Brassicaceae	3
<i>Brassica rapa</i>	3711	Brassicaceae	2
<i>Boechea stricta</i>	72658	Brassicaceae	3
<i>Capsella grandiflora</i>	264402	Brassicaceae	3
<i>Capsella rubella</i>	81985	Brassicaceae	3
<i>Eutrema salsugineum</i>	72664	Brassicaceae	4
<i>Schrenkiella parvula</i>	98039	Brassicaceae	3
<i>Beta vulgaris</i>	161934	Chenopodiaceae	2
<i>Cucumis sativus</i>	3659	Cucurbitaceae	2
<i>Ricinus communis</i>	3988	Euphorbiaceae	2
<i>Arachis ipaensis</i>	130454	Fabaceae	2
<i>Medicago truncatula</i>	3880	Fabaceae	2
<i>Phaseolus vulgaris</i>	3885	Fabaceae	2
<i>Linum usitatissimum</i>	4006	Linaceae	4
<i>Gossypium raimondii</i>	29730	Malvaceae	3
<i>Theobroma cacao</i>	3641	Malvaceae	2
<i>Musa acuminata</i>	4641	Musaceae	4
<i>Erythranthe guttata</i>	4155	Phrymaceae	2
<i>Pinus taeda</i>	3352	Pinaceae	1
<i>Brachypodium distachyon</i>	15368	Poaceae	2
<i>Oryza sativa</i>	4530	Poaceae	2
<i>Sorghum bicolor</i>	4558	Poaceae	2
<i>Setaria italica</i>	4555	Poaceae	2
<i>Zea mays</i>	4577	Poaceae	2
<i>Aquilegia coerulea</i>	218851	Ranunculaceae	1
<i>Fragaria vesca</i>	57918	Rosaceae	2

<i>Malus domestica</i>	3750	Rosaceae	5
<i>Prunus persica</i>	3760	Rosaceae	2
<i>Coffea canephora</i>	49390	Rubiaceae	2
<i>Citrus clementina</i>	85681	Rutaceae	2
<i>Citrus sinensis</i>	2711	Rutaceae	2
<i>Populus trichocarpa</i>	3694	Salicaceae	2
<i>Capsicum annuum</i>	4072	Solanaceae	3
<i>Solanum melongena</i>	4111	Solanaceae	3
<i>Solanum lycopersicum</i>	4081	Solanaceae	3
<i>Solanum tuberosum</i>	4113	Solanaceae	3
<i>Vitis vinifera</i>	29760	Vitaceae	2

---

848

849

849 **Table S2. Cryo-EM statistics and model refinement for AtMLKL tetramer**

	AtMLKL3 tetramer	AtMLKL2 tetramer
<b>Data collection and processing</b>		
Microscope	FEI Titan Krios	FEI Titan Krios
Detector	Gatan K2 Summit	Gatan K2 Summit
Voltage(kV)	300	300
Magnification	22500x	22500x
Pixel size (Å)	1.30654	1.30654
Total electron dose (e <sup>-</sup> /Å <sup>2</sup> )	50	50
Defocus range (µm)	-1.5 ~ -2.3	-1.6~-2.2
Micrographs collected	1,434	1,828
<b>Reconstruction</b>		
Total extracted particles	983,779	1,527,009
Number of particles used for 3D reconstruction	629,287	796,901
Number of particles used for refinement	123,472	154,008
Symmetry	D2	D2
Resolution (Å) 0.143 after refinement	3.84	4.51
Resolution (Å) 0.143 after post-processing	3.39	4.08
Map sharpening B-factor (Å <sup>2</sup> )	-152	-222.79
<b>Refinement</b>		
Estimated Resolution (Å)	3.4	4.1
Model composition		
Number of protein atoms	16584	14238
Number of ligand atoms	0	0
MapCC (mask/box)	0.83/0.79	0.81/0.81
Rwork/Rfree (%)	34.35/34.35	39.4/39.4
R.M.S deviations		
Bonds lengths (Å)	0.011	0.010
Bonds angles (°)	0.941	0.797
<b>Validation</b>		
MolProbity overall score	2.22	2.56
All-atom clashscore	15.96	18.07
Rotamer outliers (%)	0.67	1.57
C-beta deviations	0.0	0.0
EMRinger score	1.56	1.42
Ramachandran plot statistics		
Preferred (%)	91.27	85.27
Allowed (%)	8.33	14.31
Outlier (%)	0.40	0.42

850

851

852

853 **Table S3 Primer pairs used in this study.**

Forward primer	Sequence 5' -3'	Reverse primer	Sequence 5' -3'	Use, comments
SALK_041569c_ RP	GAGAGACAG CGAAAACCT GTG	SALK_0415 69c_LP	CTTCTCTT GCAATGCC TCAAC	Genotyping of the wild type allele of <i>AtMLKL1</i>
SALK_041569c_ RP	GAGAGACAG CGAAAACCT GTG	LBb1.3	ATTTTGCC GATTTCCG AAC	Genotyping of the mutant allele of <i>AtMLKL1</i>
SALK_124412c_ RP AT5G41730	TCAGCTTAG CTTTCAACA CGG	SALK_1244 12c_LP AT5G41730	GAAGATAC TCCATCCC CCTTG	Genotyping of the wild type allele of <i>AtMLKL2</i>
SALK_124412c_ RP AT5G41730	TCAGCTTAG CTTTCAACA CGG	LBb1.3	ATTTTGCC GATTTCCG AAC	Genotyping of the mutant allele of <i>AtMLKL2</i>
GABI_491E02_R P	TACACGAAG CCCATTAC TTC	GABI_491E 02_LP	TATTACCT CTGCGGAT TCACG	Genotyping of the wild type allele of <i>AtMLKL3</i>
GABI_o3144/35St	GTGGATTGA TGTGATATC TCC	GABI_491E 02_LP	TATTACCT CTGCGGAT TCACG	Genotyping of the mutant allele of <i>AtMLKL3</i>
AT1g64300-Fw1	CACCATGGA GCAATTCAG GCAAATCGG AGAGGTT	AT1g64300- Rv1	TGTAAGCT CAGAGTCT GAAGCAG GACCAGTT A	D-topo cloning of <i>AtMLKL1</i> cDNA without STOP codon
AT5G41730-Fw1	CACCATGGA GCAATTCAG ACAAATCGG AGAAGTTCT T	AT5G41730- Rv1	AGTAAGCT CAGAGTCT GAAGCATG ACCAGTCT GTT	D-topo cloning of <i>AtMLKL2</i> cDNA without STOP codon
D-topo- <i>AtMLKL3</i> -f	CACCATGGA TCAATTTTCG AGAGATAGG AGAGGTATT	D-topo- <i>AtMLKL3</i> - r_without_st op	GGAAAGCT CAGAGTCA GAGGCAT GT	D-topo cloning of <i>AtMLKL3</i> cDNA without STOP codon
<i>AtMLKL1</i> (S393D)- f	CCTCAGTTA AGAATCAGG ATTTTTCTCG GGCTTCC	<i>AtMLKL1</i> (S3 93D)-r	GGAAGCC CGAGAAAA ATCCTGAT TCTTAACT GAGG	Site-directed mutagenesis to obtain <i>AtMLKL1</i> (S393D) variant
<i>AtMLKL1</i> (S395D)- f	GTTAAGAAT CAGTCTTTT GATCGGGCT TCCTCTAGA C	<i>AtMLKL1</i> (S3 95D)-r	GTCTAGAG GAAGCCC GATCAAAA GACTGATT CTTAAC	Site-directed mutagenesis to obtain <i>AtMLKL1</i> (S395D) variant
AT5G41730_(S39 4D)-f	GTCGTTAAA GCGCAGGAT TCCTCGAAA CCAG	AT5G41730 _(S394D)-r	CTGGTTTC GAGGAATC CTGCGCTT TAACGAC	Site-directed mutagenesis to obtain <i>AtMLKL2</i> (S394D) variant
AT5G41730_(S39 5D)-f	CGTTAAAGC GCAGTCTGA TTCGAAACC AGGCACTCC	AT5G41730 _(S395D)-r	GGAGTGC CTGGTTTC GAATCAGA CTGCGCTT TAACG	Site-directed mutagenesis to obtain <i>AtMLKL2</i> (S395D) variant
<i>AtMLKL3</i> (S392D)- f	GTTGAATTC TGTC AAGGG ATTGATAG TAAAAGTGC TTCTTTGAC G	<i>AtMLKL3</i> (S3 92D)-r	CGTCAAAG AAGCACTT TTACTATC GAATCCCT TGACAGAA TTCAAC	Site-directed mutagenesis to obtain <i>AtMLKL3</i> (S392D) variant
<i>AtMLKL3</i> (S393D )f	CTGTCAAGG GATTCTCTG ATAAAAGTG CTTCTTTGA C	<i>AtMLKL3</i> (S3 93D)-r	GTC AAAGA AGCACTTT TATCAGAG AATCCCTT GACAG	Site-directed mutagenesis to obtain <i>AtMLKL3</i> (S393D) variant
Genomic of	CACCCCTTG	Genomic of	TGTAAGCT	D-topo cloning of genomic fragments

At3g21215-f	GAATCCACC CATACCACC AG	At3g21215-r	GAGGAGG AGGATGGT GATGA	qPCR quantification of the Arabidopsis DNA
-------------	------------------------------	-------------	------------------------------	--

854

855

856

## 856 Supplemental References

- 857 1. N. Kleinboelting, G. Huet, A. Kloetgen, P. Viehoveer, B. Weisshaar,  
858 GABI-Kat SimpleSearch: new features of the Arabidopsis thaliana T-  
859 DNA mutant database. *Nucleic Acids Res* **40**, D1211-1215 (2012).
- 860 2. J. M. Alonso *et al.*, Genome-wide insertional mutagenesis of  
861 Arabidopsis thaliana. *Science* **301**, 653-657 (2003).
- 862 3. M. Bartsch *et al.*, Salicylic acid-independent ENHANCED DISEASE  
863 SUSCEPTIBILITY1 signaling in Arabidopsis immunity and cell death is  
864 regulated by the monooxygenase FMO1 and the Nudix hydrolase  
865 NUDT7. *Plant Cell* **18**, 1038-1051 (2006).
- 866 4. T. Nakagawa *et al.*, Improved Gateway binary vectors: high-  
867 performance vectors for creation of fusion constructs in transgenic  
868 analysis of plants. *Biosci Biotechnol Biochem* **71**, 2095-2100 (2007).
- 869 5. S. J. Clough, A. F. Bent, Floral dip: a simplified method for  
870 Agrobacterium-mediated transformation of Arabidopsis thaliana. *Plant*  
871 *J* **16**, 735-743 (1998).
- 872 6. C. Koncz, J. Schell, The promoter of TL-DNA gene 5 controls the  
873 tissue-specific expression of chimaeric genes carried by a novel type of  
874 Agrobacterium binary vector. *Molecular and General Genetics MGG*  
875 **204**, 383-396 (1986).
- 876 7. F. Jacob *et al.*, A dominant-interfering camta3 mutation compromises  
877 primary transcriptional outputs mediated by both cell surface and  
878 intracellular immune receptors in Arabidopsis thaliana. *New Phytol* **217**,  
879 1667-1680 (2018).
- 880 8. P. Bucher, K. Karplus, N. Moeri, K. Hofmann, A flexible motif search  
881 technique based on generalized profiles. *Comput Chem* **20**, 3-23  
882 (1996).
- 883 9. K. Katoh, K. Misawa, K. Kuma, T. Miyata, MAFFT: a novel method for  
884 rapid multiple sequence alignment based on fast Fourier transform.  
885 *Nucleic Acids Res* **30**, 3059-3066 (2002).
- 886 10. J. Soding, Protein homology detection by HMM-HMM comparison.  
887 *Bioinformatics* **21**, 951-960 (2005).
- 888 11. D. Lapin *et al.*, A coevolved EDS1-SAG101-NRG1 module mediates  
889 cell death signaling by TIR-domain immune receptors. *bioRxiv*, 572826  
890 (2019).
- 891 12. T. Maekawa *et al.*, Subfamily-Specific Specialization of RGH1/MLA  
892 Immune Receptors in Wild Barley. *Mol Plant Microbe Interact* **32**, 107-  
893 119 (2019).
- 894 13. S. Q. Zheng *et al.*, MotionCor2: anisotropic correction of beam-induced  
895 motion for improved cryo-electron microscopy. *Nat Methods* **14**, 331-  
896 332 (2017).
- 897 14. A. Rohou, N. Grigorieff, CTFFIND4: Fast and accurate defocus  
898 estimation from electron micrographs. *J Struct Biol* **192**, 216-221  
899 (2015).
- 900 15. J. Zivanov *et al.*, New tools for automated high-resolution cryo-EM  
901 structure determination in RELION-3. *Elife* **7**, (2018).
- 902 16. A. Brown *et al.*, Tools for macromolecular model building and  
903 refinement into electron cryo-microscopy reconstructions. *Acta*  
904 *Crystallogr D Biol Crystallogr* **71**, 136-153 (2015).



- 905 17. P. D. Adams *et al.*, PHENIX: a comprehensive Python-based system  
906 for macromolecular structure solution. *Acta Crystallogr D Biol*  
907 *Crystallogr* **66**, 213-221 (2010).
- 908 18. L. Su *et al.*, A plug release mechanism for membrane permeation by  
909 MLKL. *Structure* **22**, 1489-1500 (2014).
- 910 19. J. M. Murphy *et al.*, The pseudokinase MLKL mediates necroptosis via  
911 a molecular switch mechanism. *Immunity* **39**, 443-453 (2013).
- 912 20. I. M. Saur *et al.*, Multiple pairs of allelic MLA immune receptor-powdery  
913 mildew AVRAs argue for a direct recognition mechanism. *Elife*  
914 **8**, (2019).
- 915 21. T. Maekawa *et al.*, Coiled-coil domain-dependent homodimerization of  
916 intracellular barley immune receptors defines a minimal functional  
917 module for triggering cell death. *Cell Host Microbe* **9**, 187-199 (2011).
- 918 22. F. Vogler, S. S. Konrad, S. Sprunck, Knockin' on pollen's door: live cell  
919 imaging of early polarization events in germinating Arabidopsis pollen.  
920 *Front Plant Sci* **6**, 246 (2015).
- 921 23. T. Hamada *et al.*, Purification and characterization of novel  
922 microtubule-associated proteins from Arabidopsis cell suspension  
923 cultures. *Plant Physiol* **163**, 1804-1816 (2013).
- 924 24. S. Fujita *et al.*, An atypical tubulin kinase mediates stress-induced  
925 microtubule depolymerization in Arabidopsis. *Curr Biol* **23**, 1969-1978  
926 (2013).
- 927 25. C. Gehl *et al.*, Quantitative analysis of dynamic protein-protein  
928 interactions in planta by a floated-leaf luciferase complementation  
929 imaging (FLuCI) assay using binary Gateway vectors. *Plant J* **67**, 542-  
930 553 (2011).
- 931 26. S. D. Yoo, Y. H. Cho, J. Sheen, Arabidopsis mesophyll protoplasts: a  
932 versatile cell system for transient gene expression analysis. *Nat Protoc*  
933 **2**, 1565-1572 (2007).
- 934 27. R. Wessling, R. Panstruga, Rapid quantification of plant-powdery  
935 mildew interactions by qPCR and conidiospore counts. *Plant Methods*  
936 **8**, 35 (2012).
- 937 28. A. Cabral *et al.*, Identification of *Hyaloperonospora arabidopsidis*  
938 transcript sequences expressed during infection reveals isolate-specific  
939 effectors. *PLoS One* **6**, e19328 (2011).
- 940 29. S. Bai *et al.*, Structure-function analysis of barley NLR immune  
941 receptor MLA10 reveals its cell compartment specific activity in cell  
942 death and disease resistance. *PLoS Pathog* **8**, e1002752 (2012).
- 943 30. R. P. Birkenbihl, C. Diezel, I. E. Somssich, Arabidopsis WRKY33 is a  
944 key transcriptional regulator of hormonal and metabolic responses  
945 toward *Botrytis cinerea* infection. *Plant Physiol* **159**, 266-285 (2012).
- 946 31. C. Gachon, P. Saindrenan, Real-time PCR monitoring of fungal  
947 development in Arabidopsis thaliana infected by *Alternaria brassicicola*  
948 and *Botrytis cinerea*. *Plant Physiol Biochem* **42**, 367-371 (2004).
- 949 32. Q. H. Shen *et al.*, Recognition specificity and RAR1/SGT1 dependence  
950 in barley Mla disease resistance genes to the powdery mildew fungus.  
951 *Plant Cell* **15**, 732-744 (2003).
- 952 33. J. Marc *et al.*, A GFP-MAP4 reporter gene for visualizing cortical  
953 microtubule rearrangements in living epidermal cells. *Plant Cell* **10**,  
954 1927-1940 (1998).

955 34. J. Riedl *et al.*, Lifeact: a versatile marker to visualize F-actin. *Nat*  
956 *Methods* **5**, 605-607 (2008).

957

958

959

960

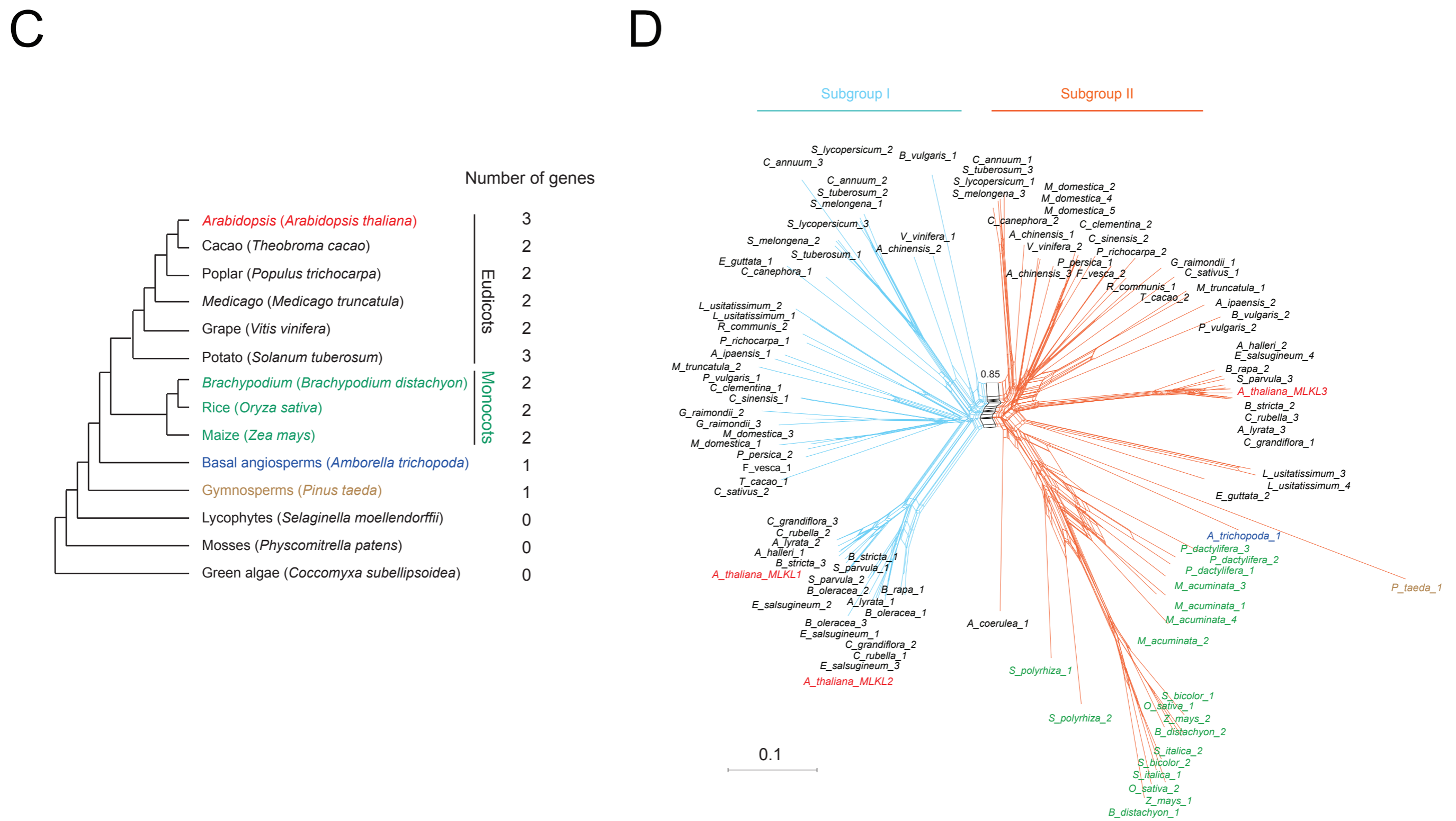
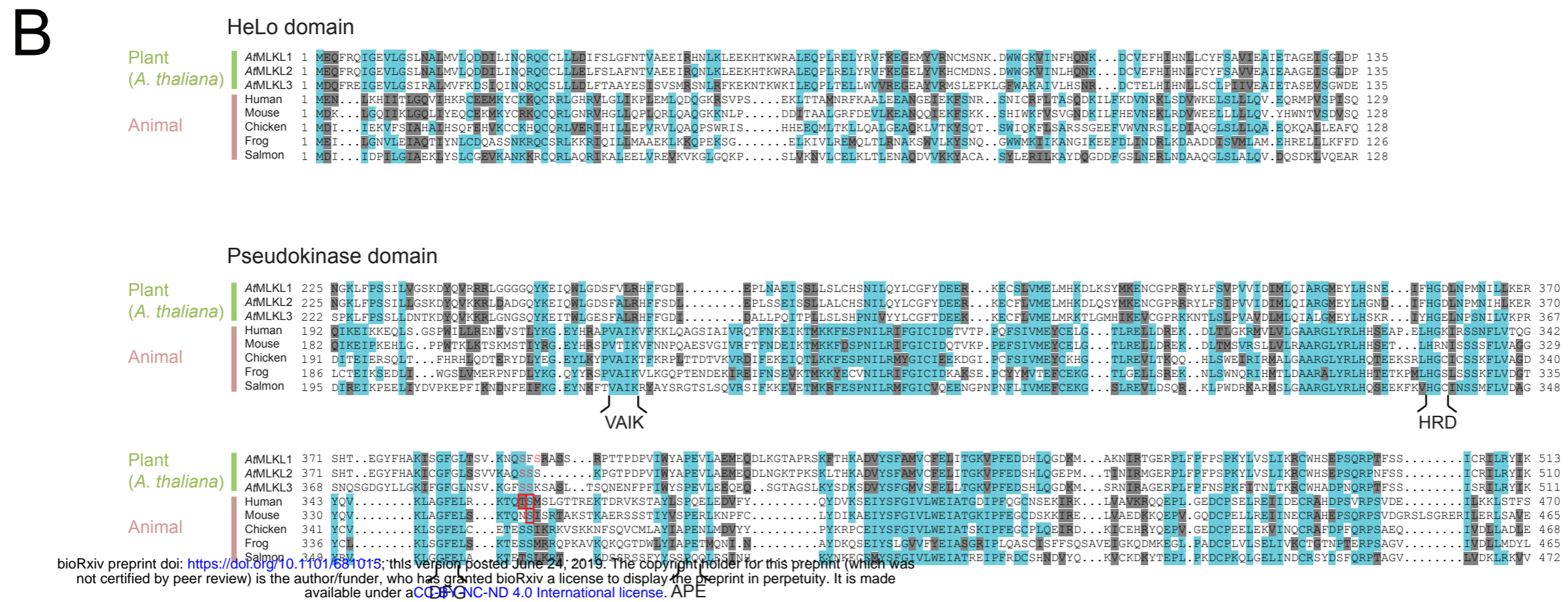
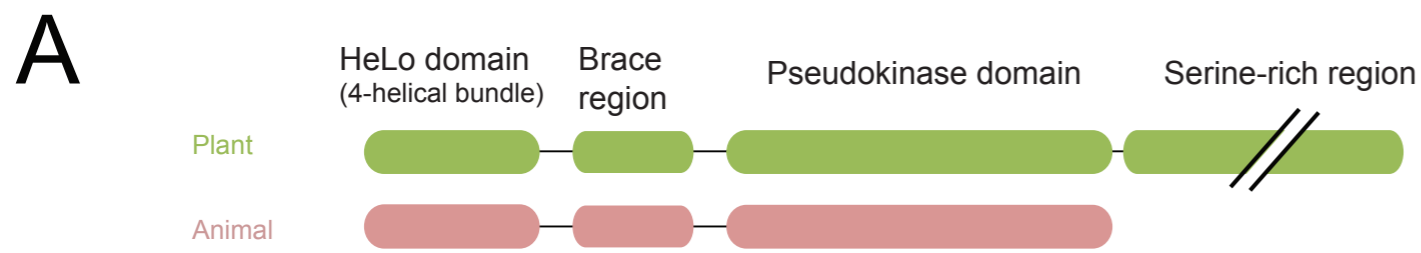


Figure 1

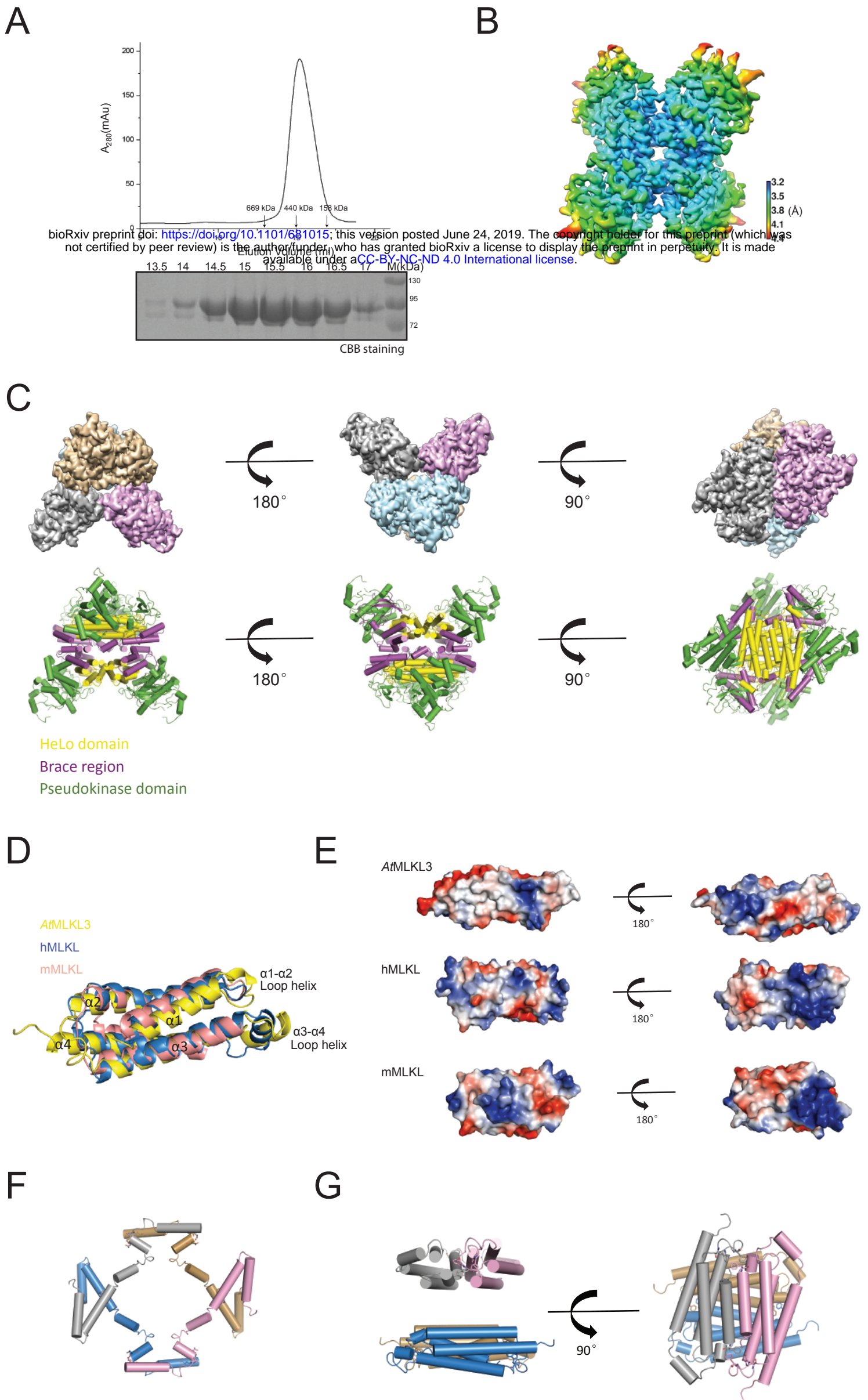
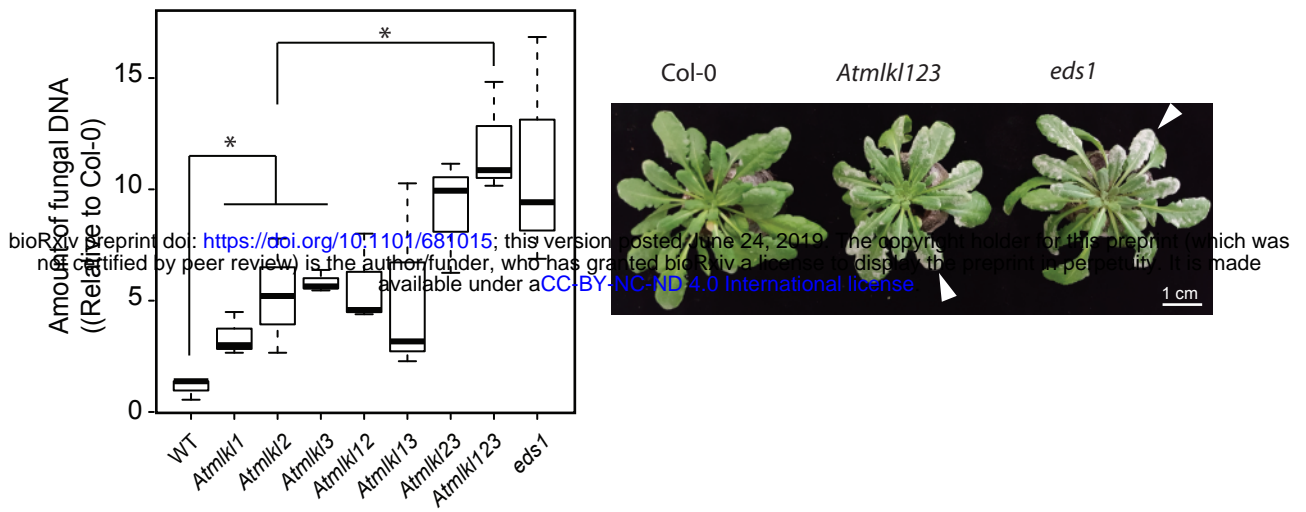


Figure 2



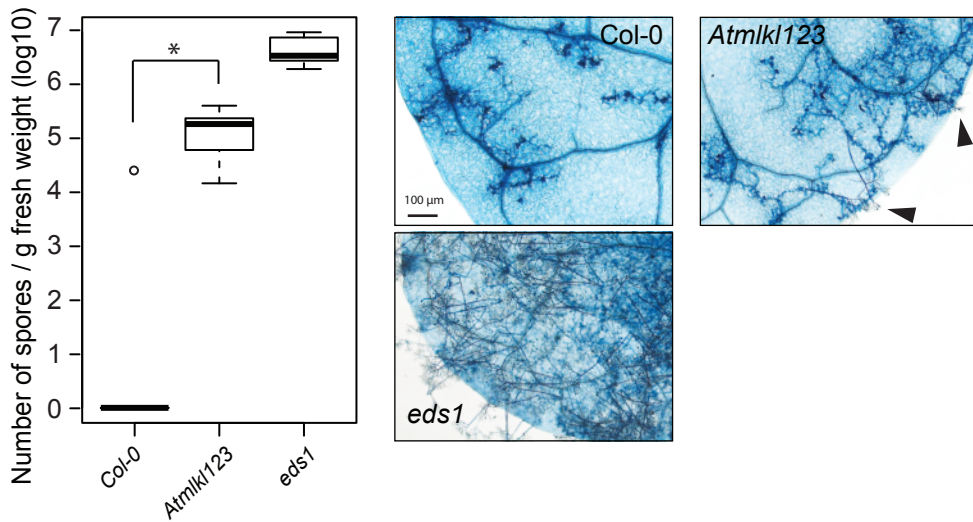
A

*G. orontii*



B

*H. arabidopsidis Emwa1*



C

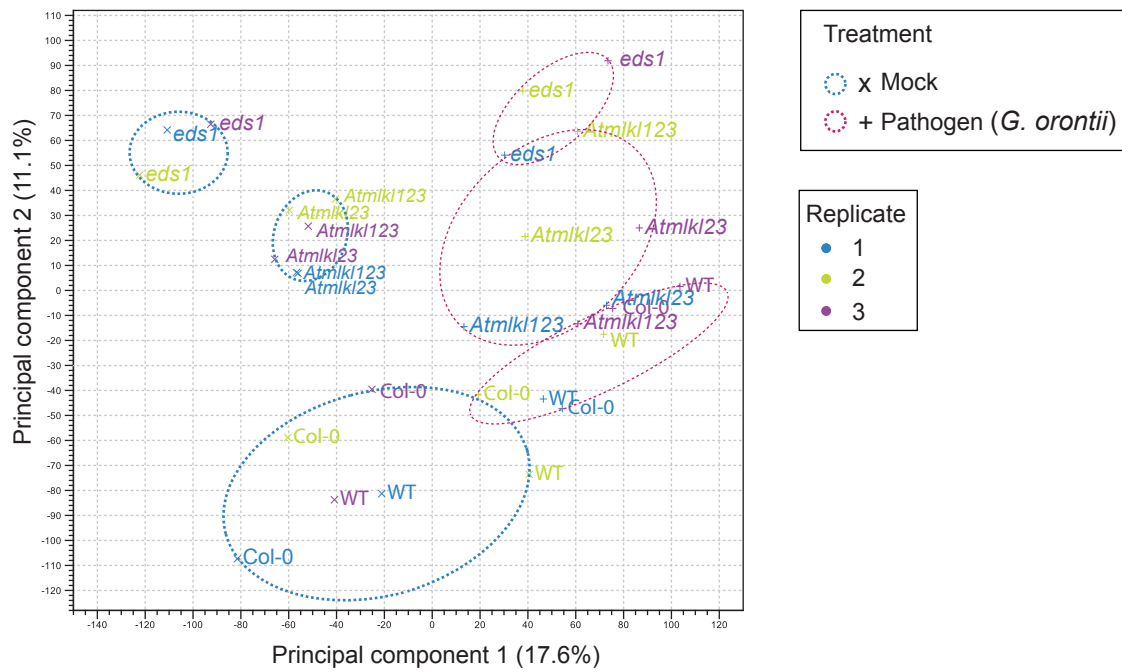
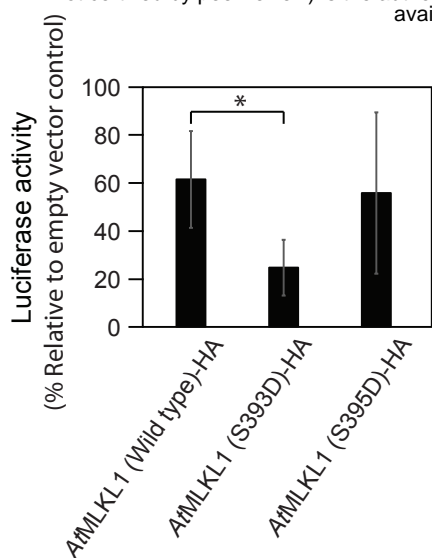
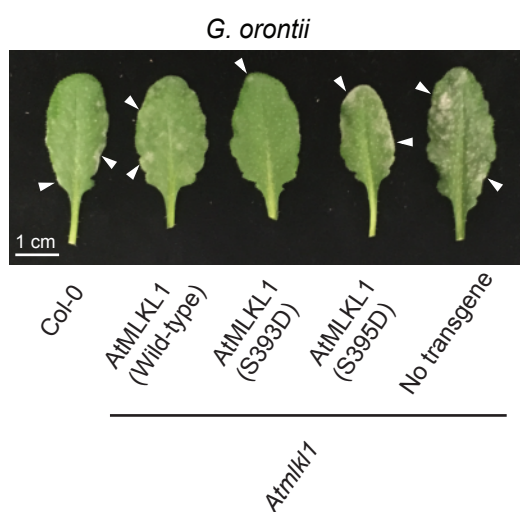


Figure 3

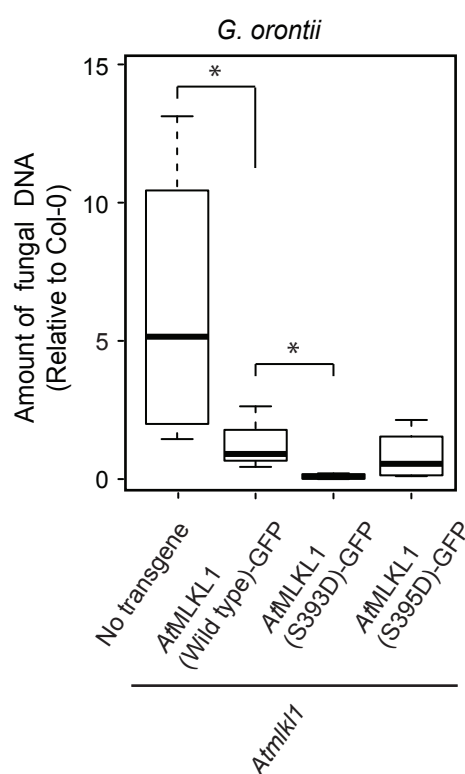
**A**



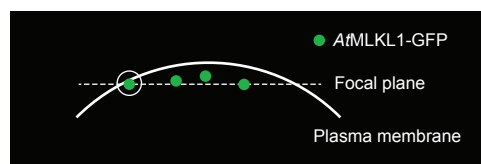
**B**



**C**



**D**



**E**

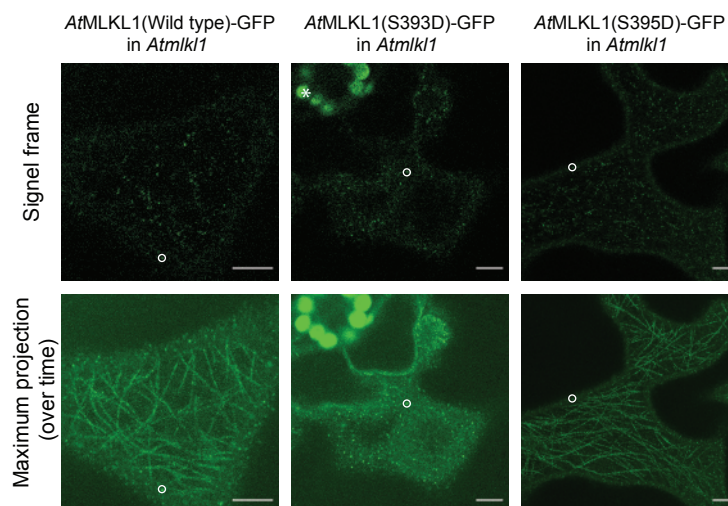


**Figure 4**

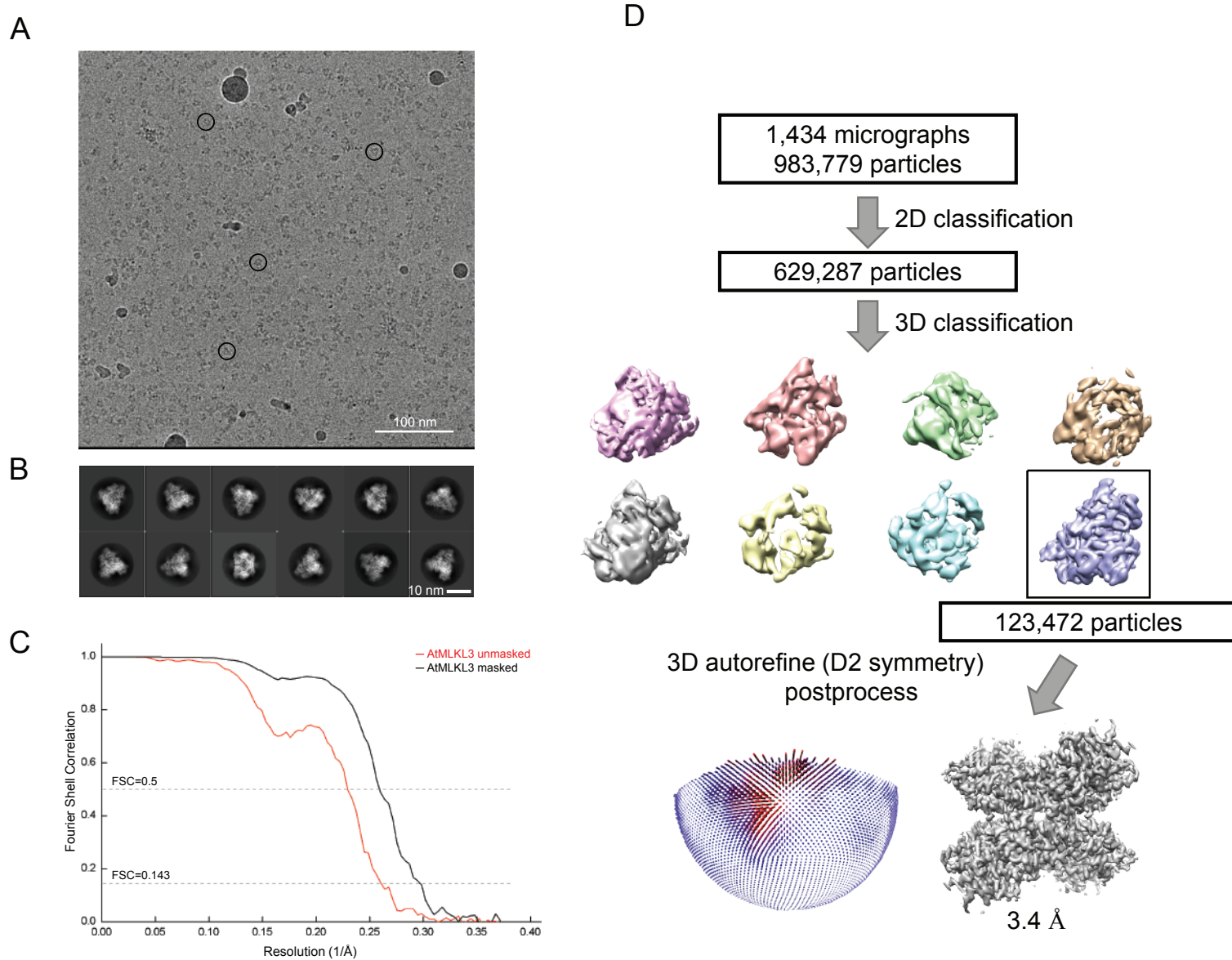


Figure S1

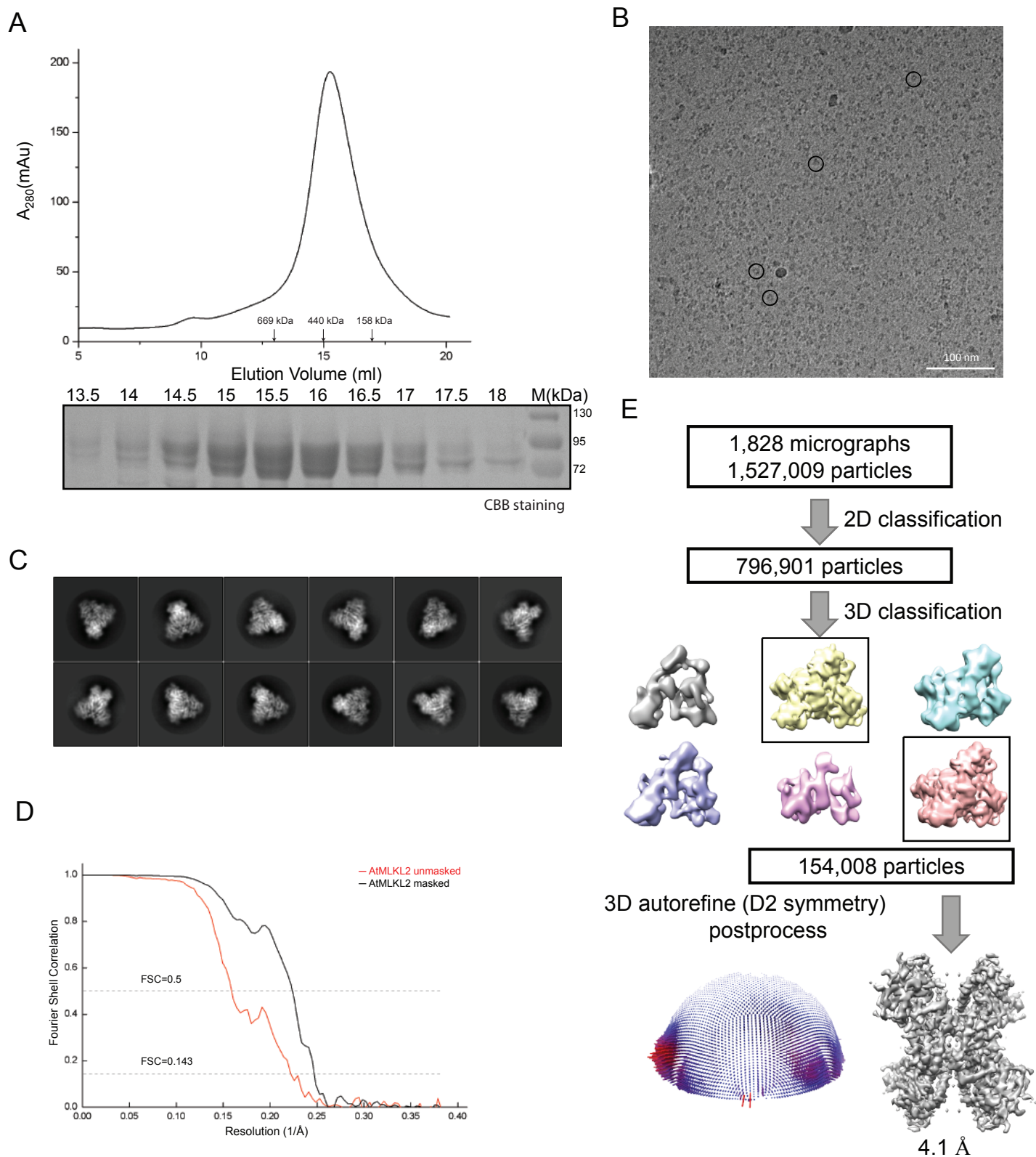
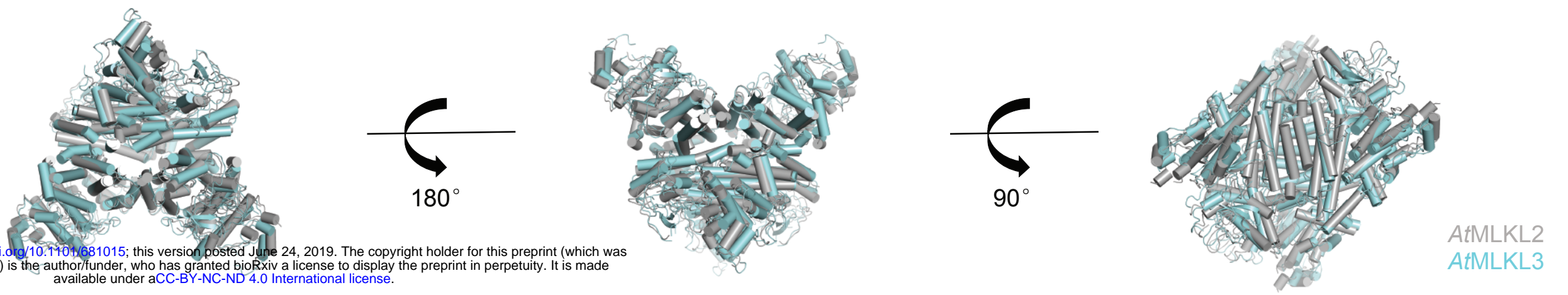


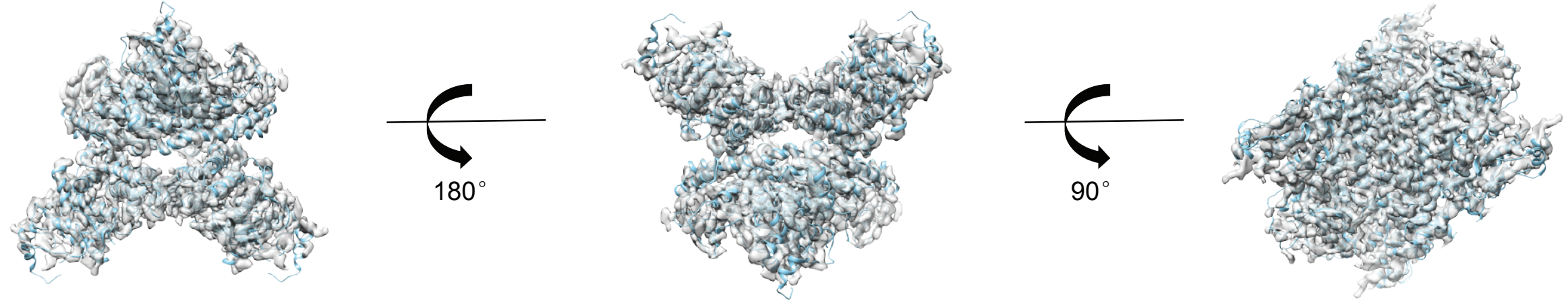
Figure S2



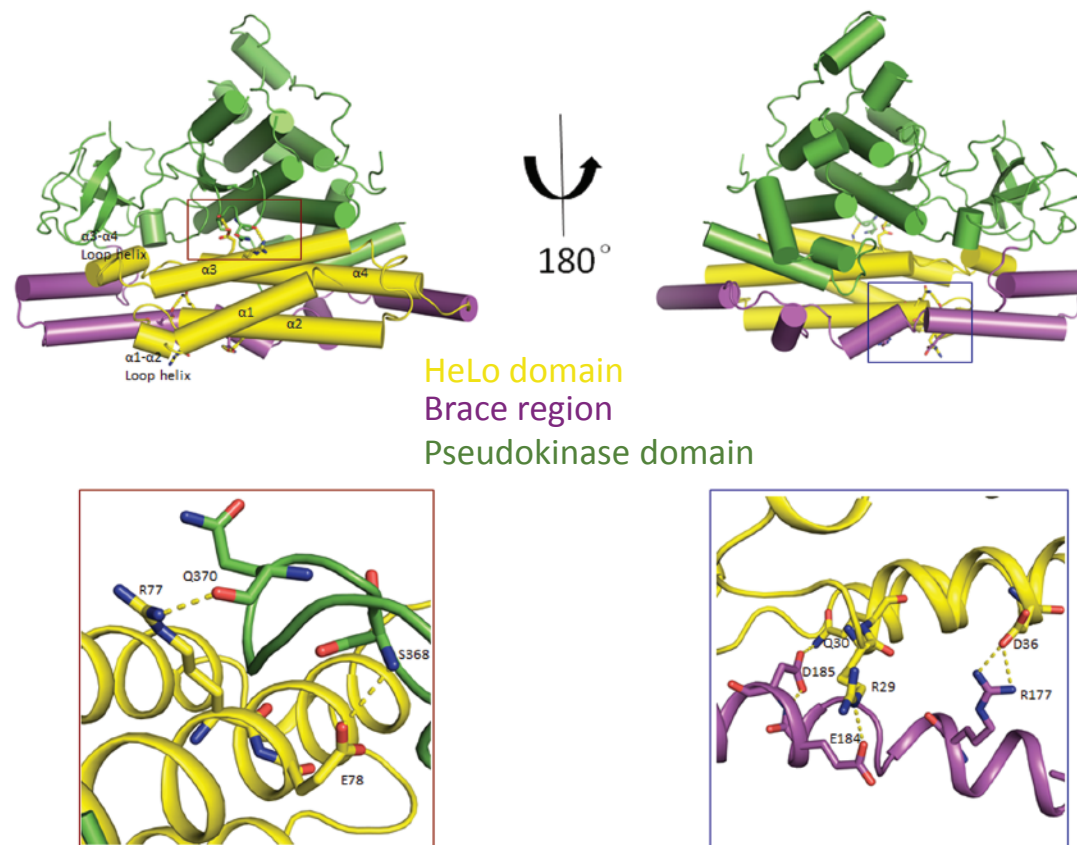
A



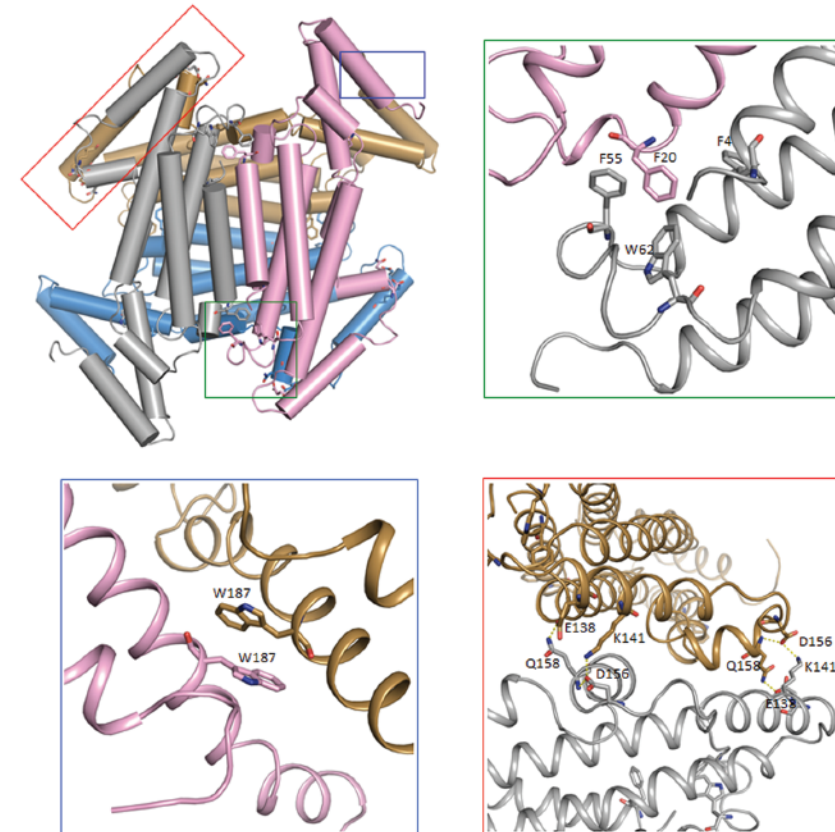
B



C

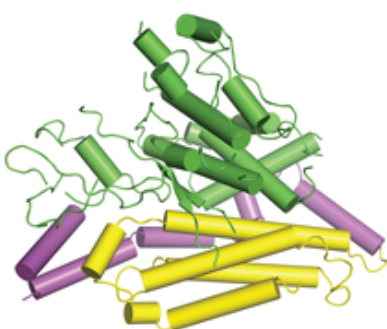


E

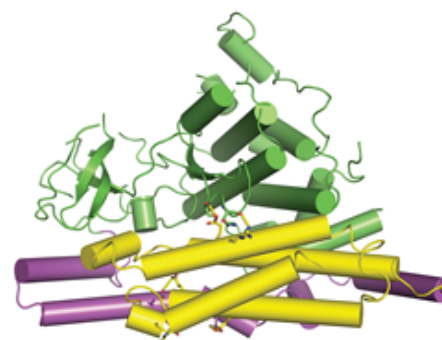


D

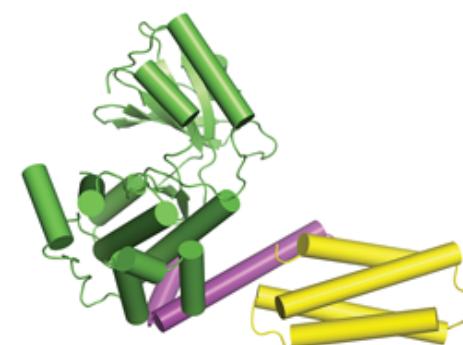
Monomer AtMLKL2



Monomer AtMLKL3



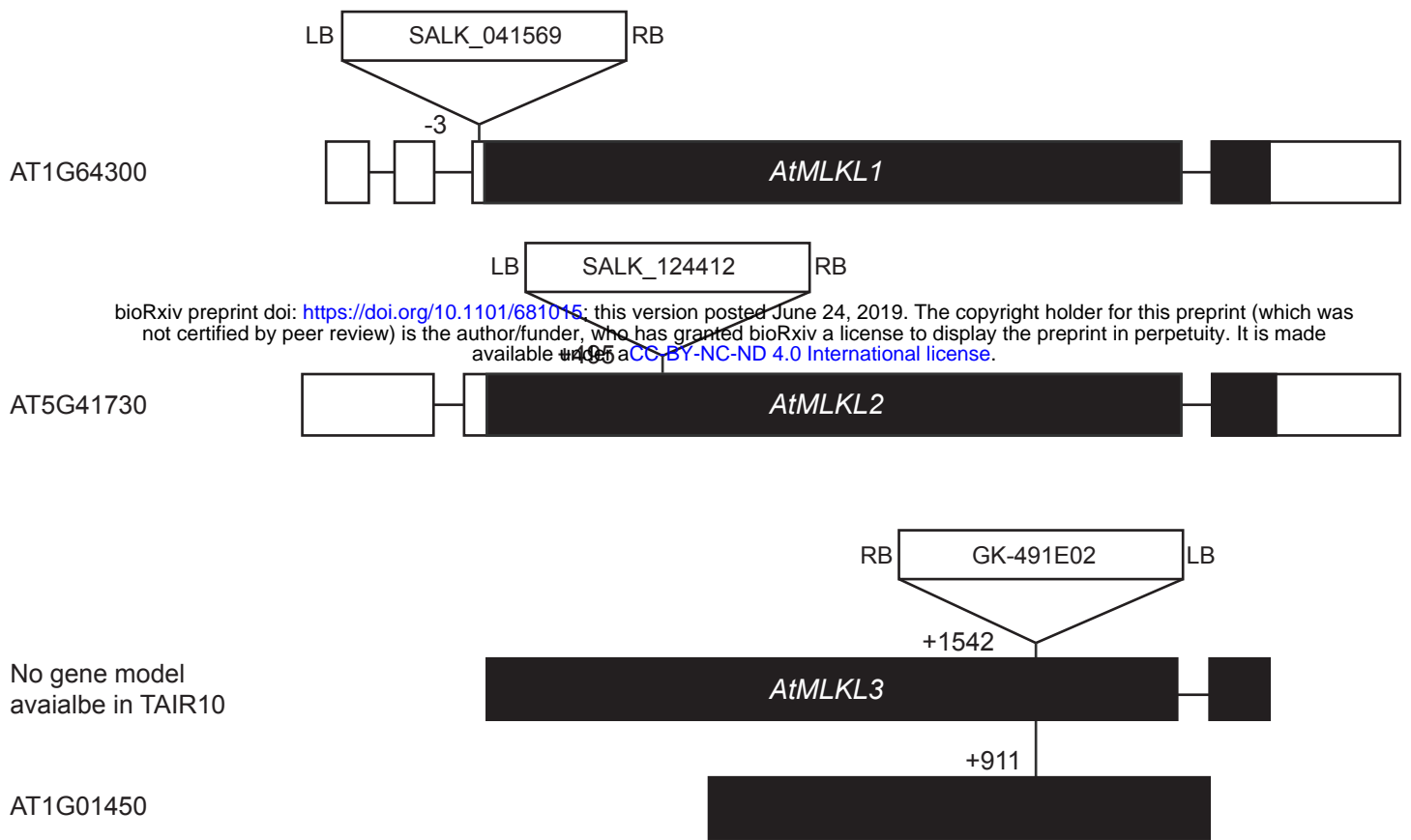
Monomer mMLKL



HeLo domain  
Brace region  
Pseudokinase domain

Figure S3

A



B



Figure S4

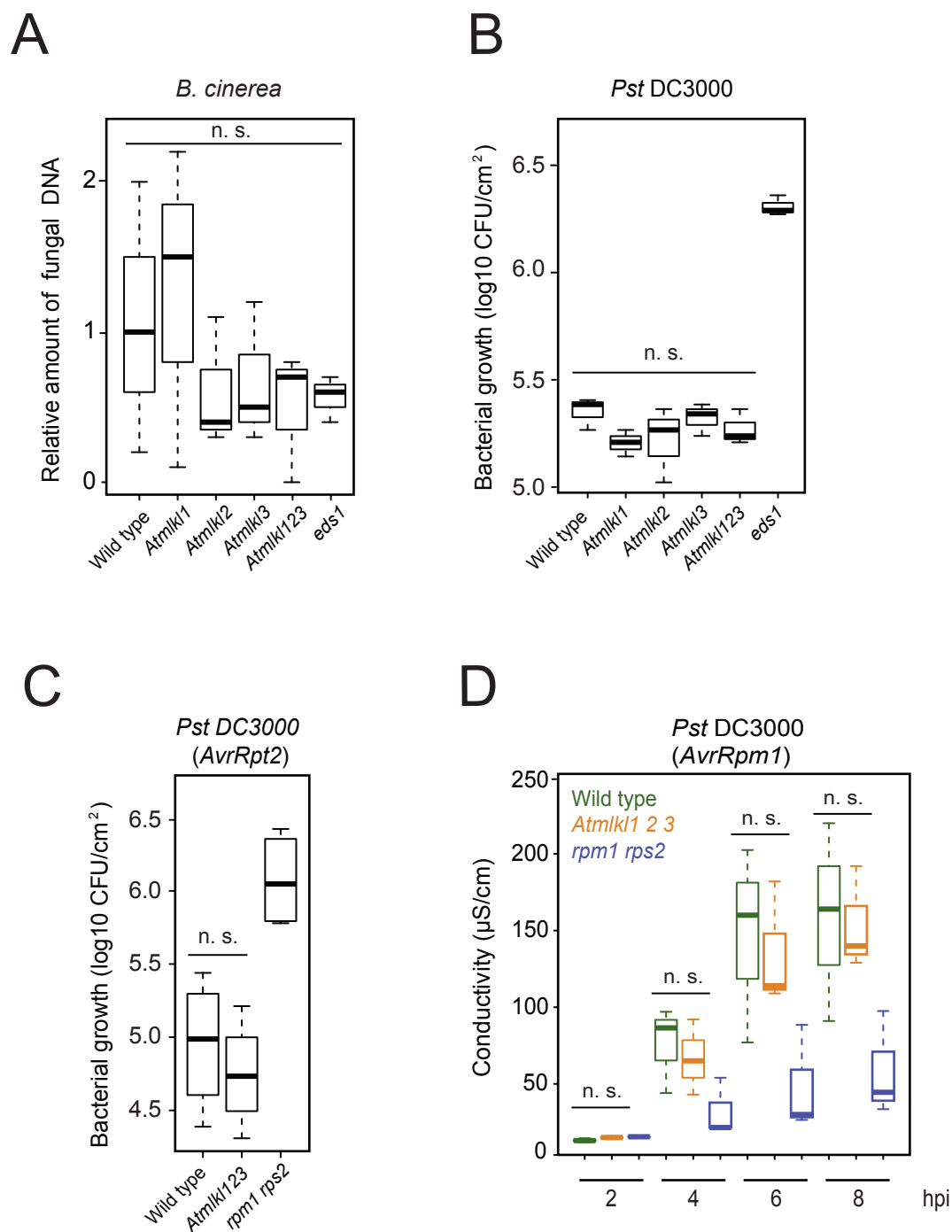


Figure S5



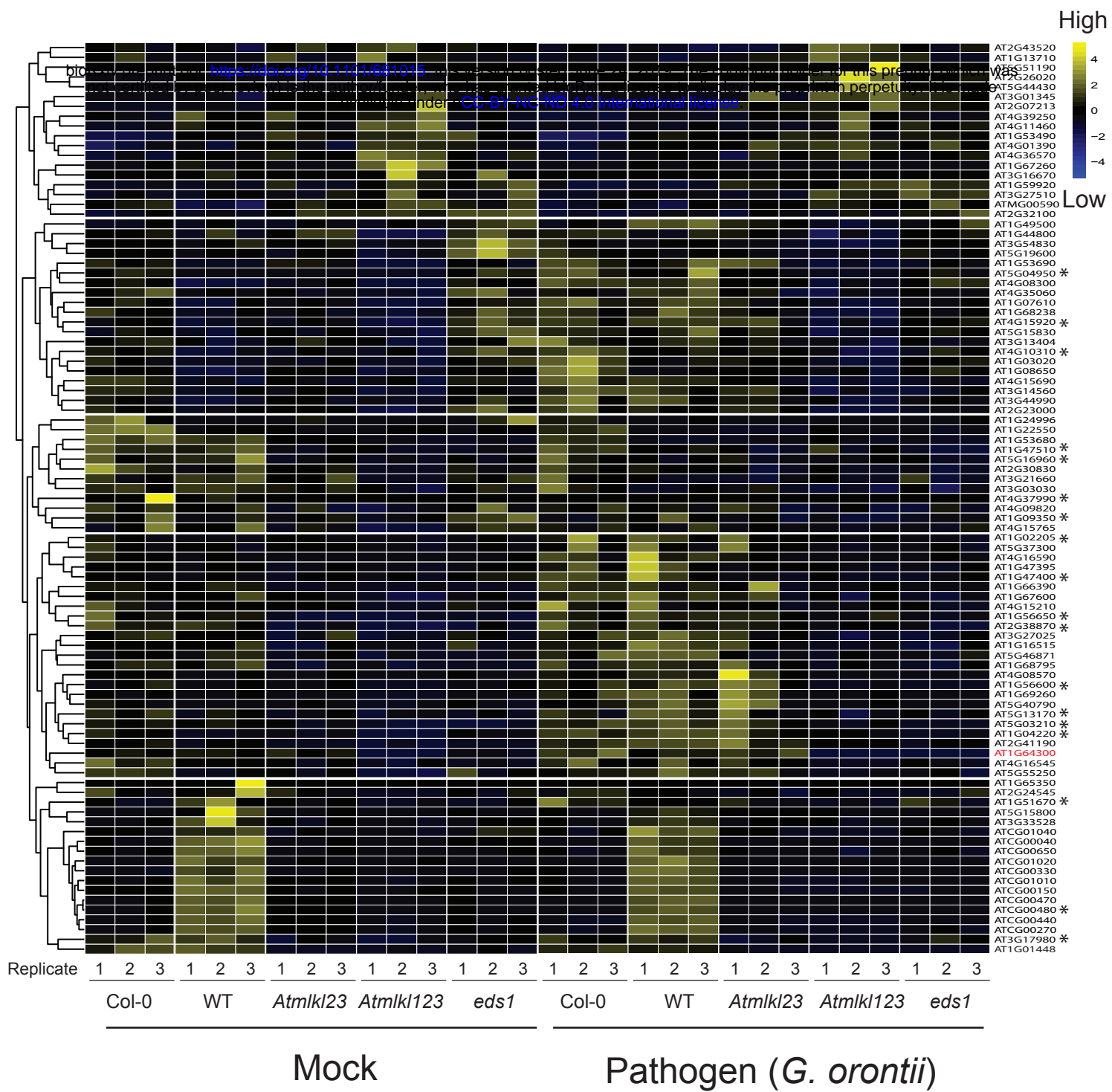
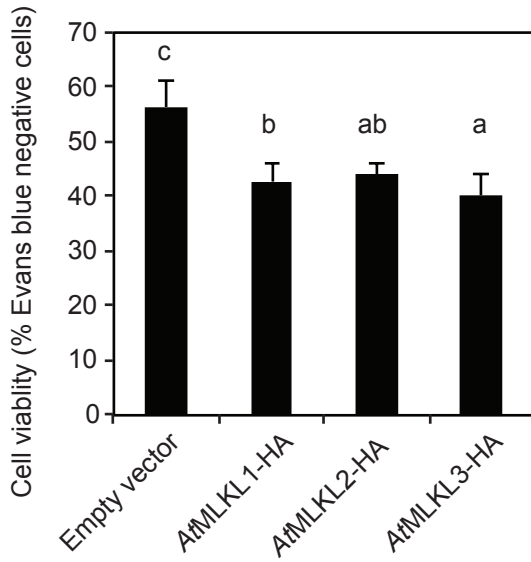
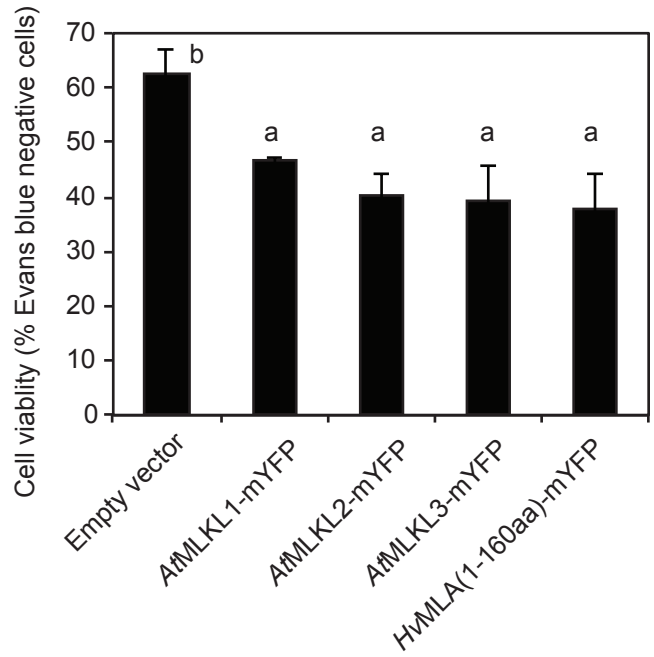


Figure S6

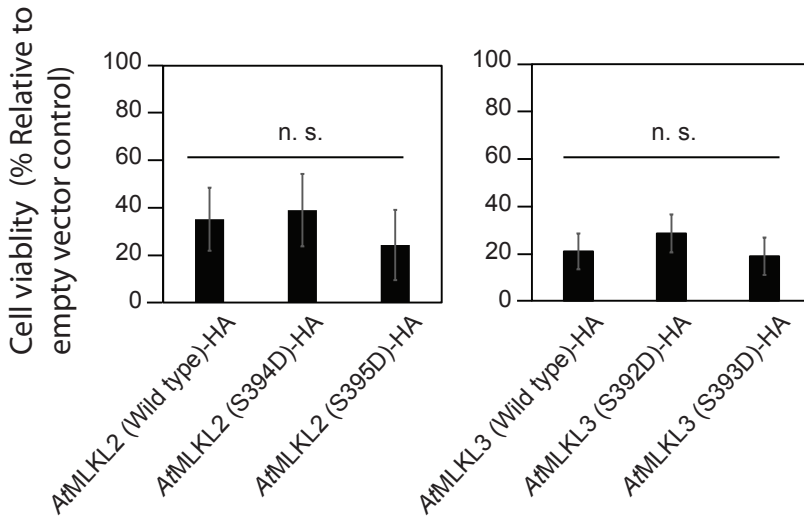
A



B



C



D

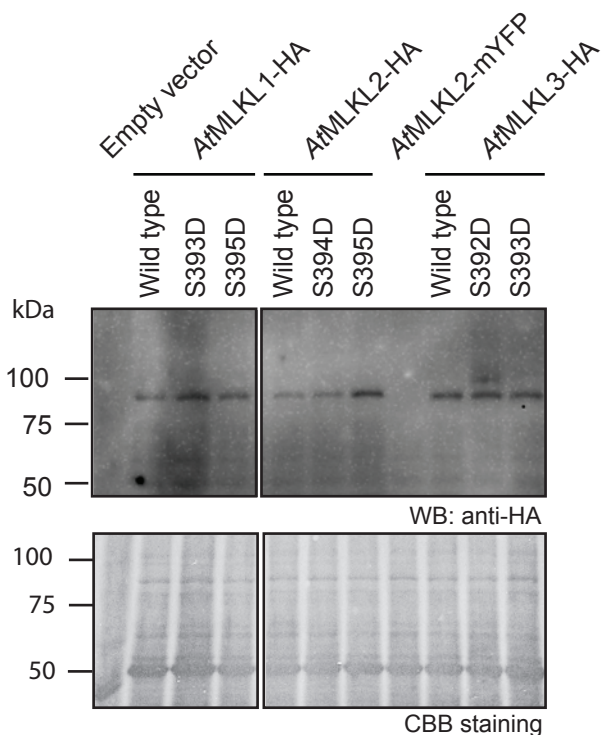
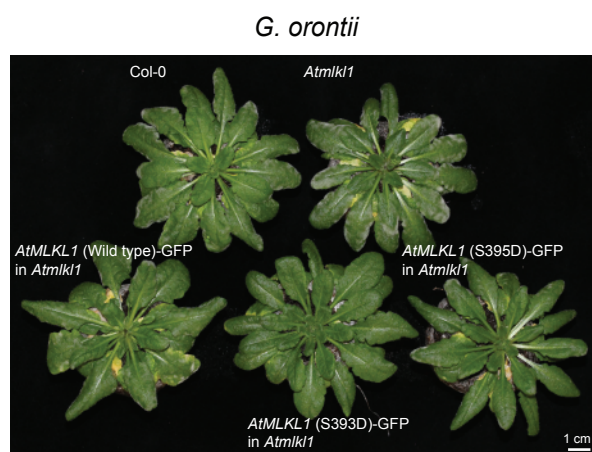


Figure S7

A



B

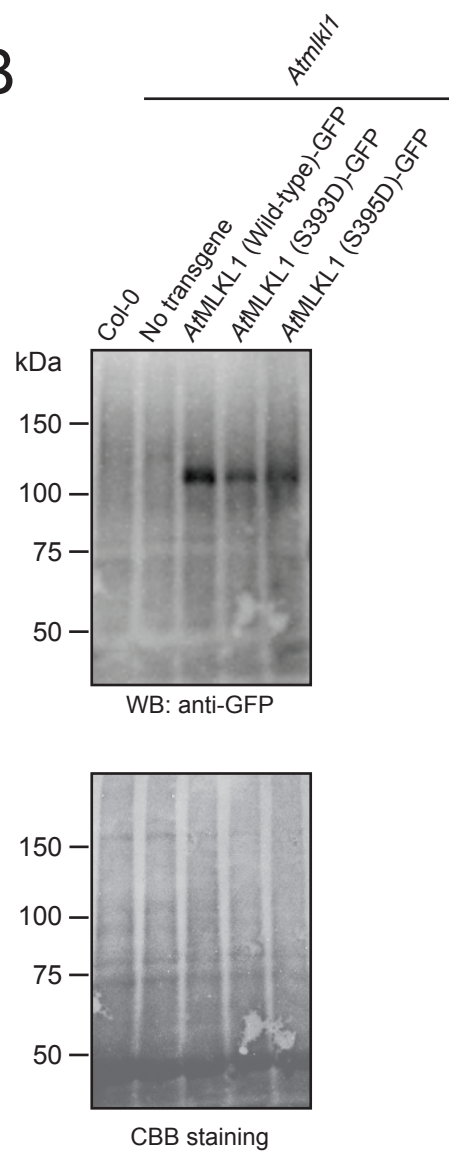
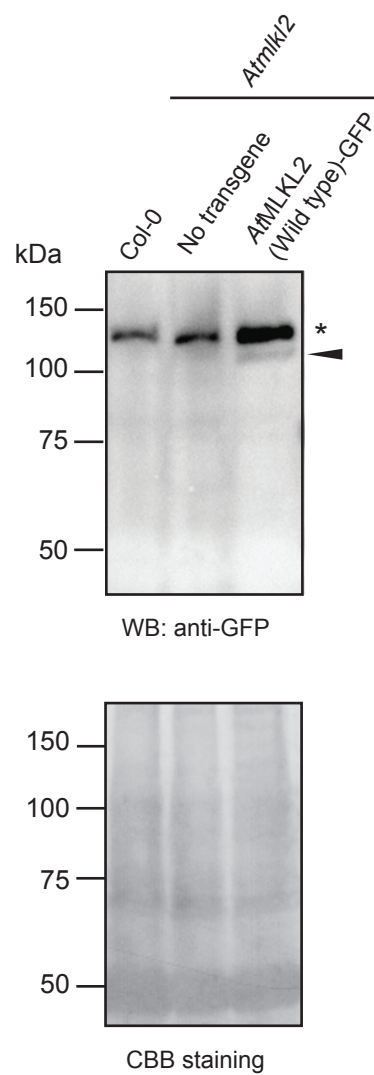


Figure S8

A



B



C

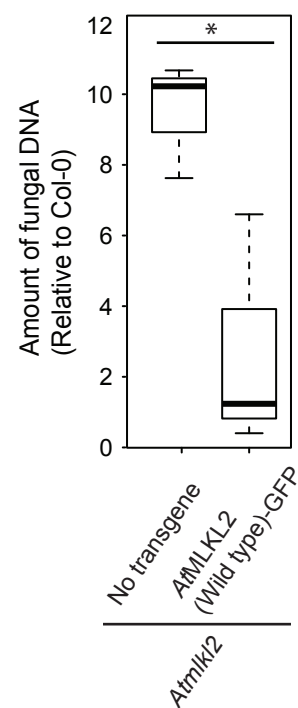


Figure S9

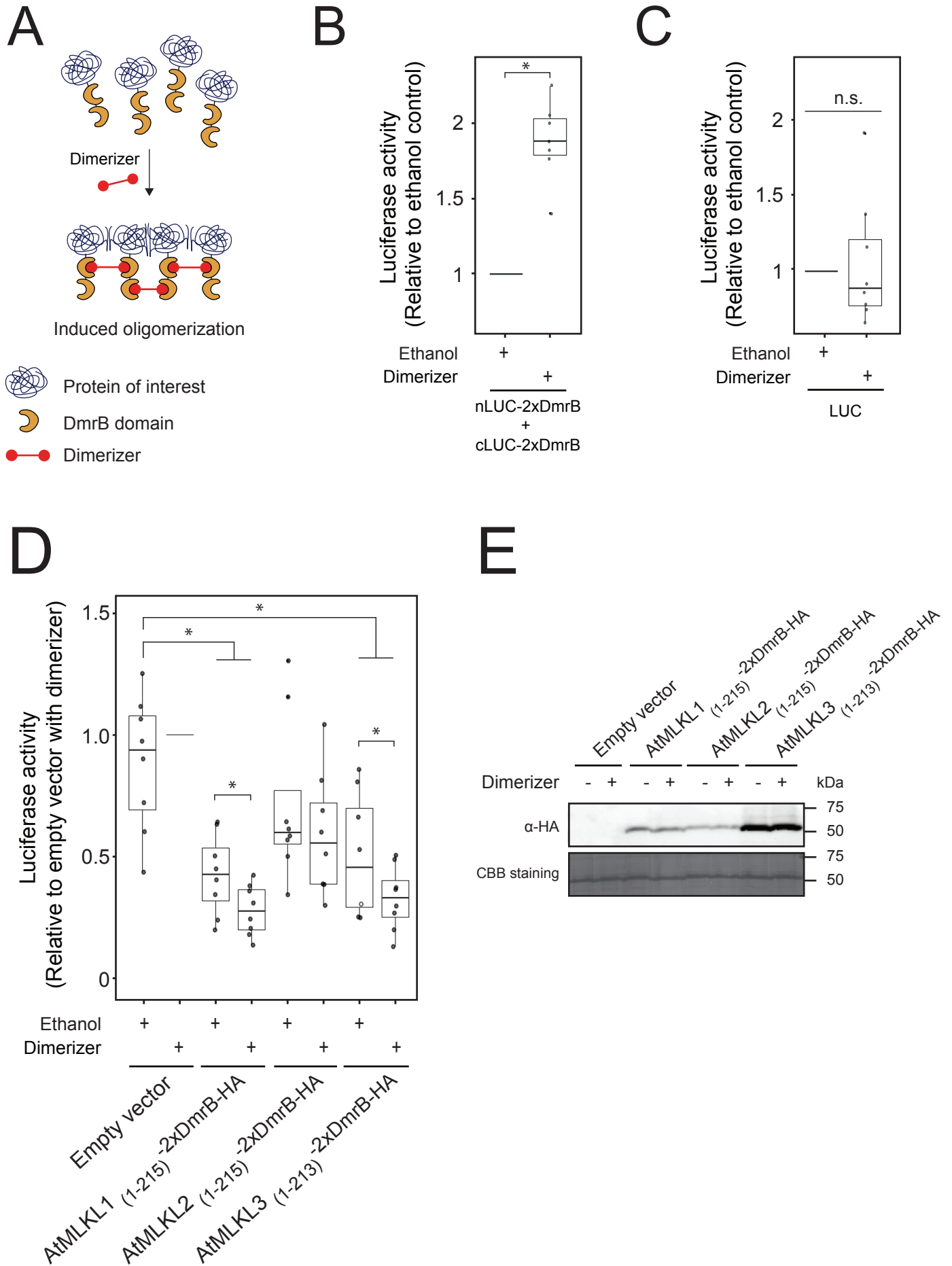
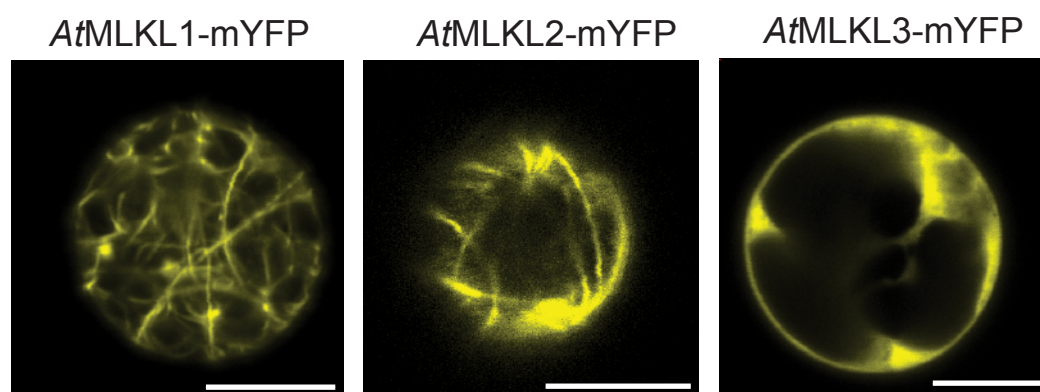


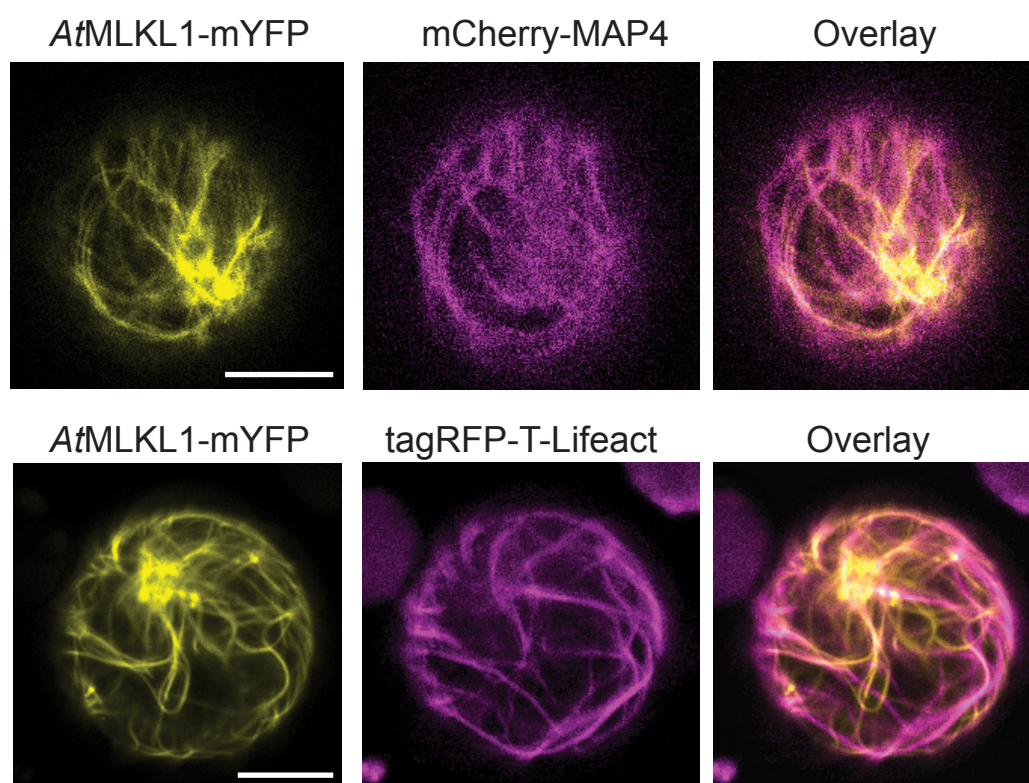
Figure S10



A



B



C

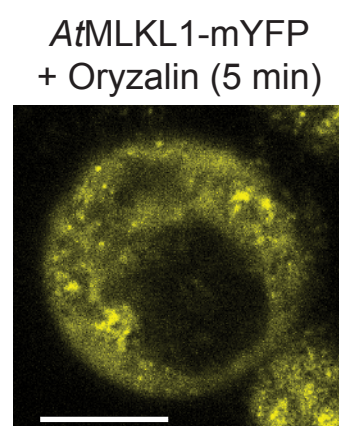
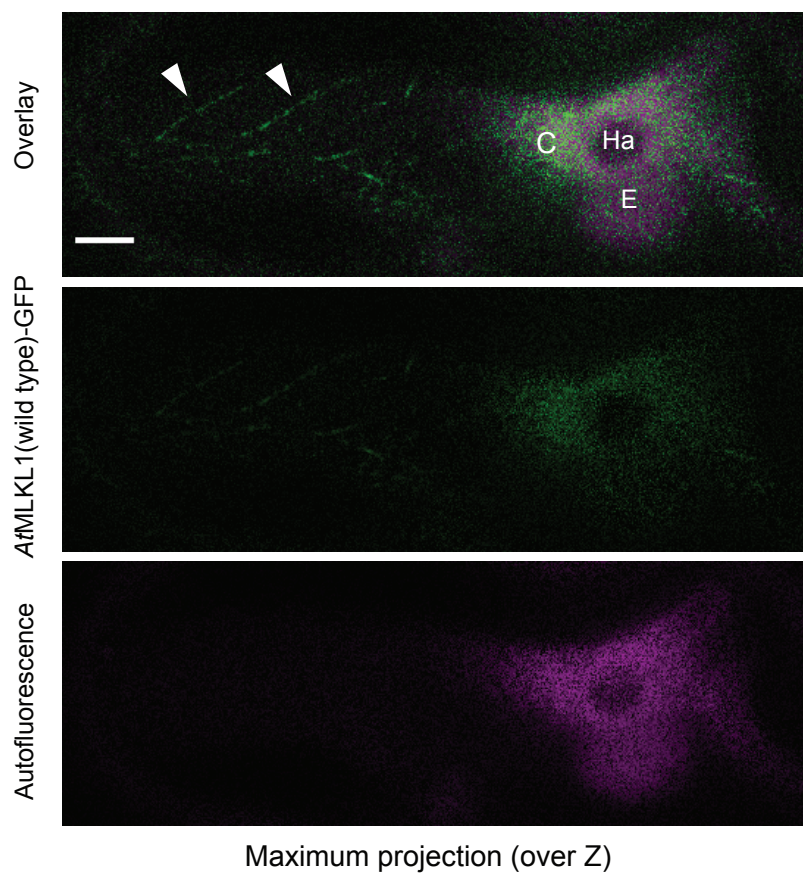


Figure S11

### *AtMLKL1*(Wild type)-GFP in *Atmlk1*



# Figure S12



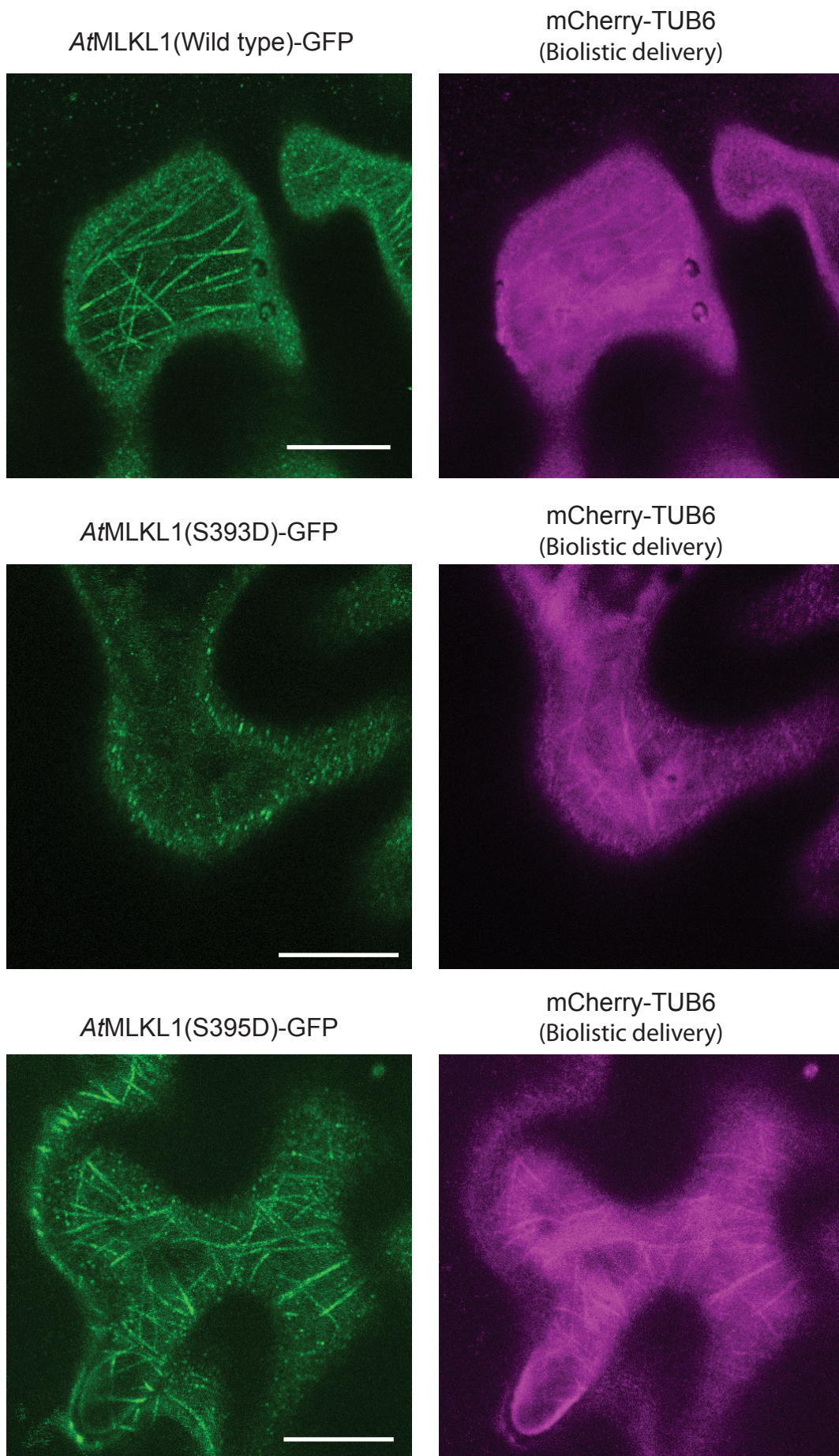


Figure S13